Temporal Structures in Electron Spectra and Charge Sign Effects in Galactic Cosmic Rays
- SUPPLEMENTAL MATERIAL -

(AMS Collaboration)

For references see the main text.

Detector.—AMS is a general purpose high energy particle physics detector in space. The layout of the detector is shown in Fig. S1. The main elements are the permanent magnet, the silicon tracker, four planes of time of flight (TOF) scintillation counters, the array of anticoincidence counters (ACCs), a transition radiation detector (TRD), a ring imaging Čerenkov detector (RICH), and an electromagnetic calorimeter (ECAL). The three-dimensional imaging capability of the 17 radiation length ECAL allows for an accurate measurement of the energy E and the shower shape of $e^{\pm}$. The AMS coordinate system is concentric with the magnet. The x axis is parallel to the main component of the magnetic field and the z axis points vertically with $z = 0$ at the center of the magnet. The (y-z) plane is the bending plane. Above, below, and downward- going refer to the AMS coordinate system. The central field of the magnet is 1.4 kG. Before flight, the field was measured in 120 000 locations to an accuracy of better than 2 G. On orbit, the magnet temperature varies from -3 to $+25$°C. The field strength is corrected with a measured temperature dependence of $-0.09\%/°$C. The tracker has nine layers, the first ($L1$) at the top of the detector, the second ($L2$) just above the magnet, six ($L3$ to $L8$) within the bore of the magnet, and the last ($L9$) just above the ECAL. $L2$ to $L8$ constitute the inner tracker. Each layer contains double-sided silicon microstrip detectors which independently measure the x and y coordinates. The tracker accurately determines the trajectory of cosmic rays by multiple measurements of the coordinates with a resolution in each layer of 10 μm for $|Z|$=1 particles in the bending (y) direction. Together, the tracker and the magnet measure the rigidity R of charged cosmic rays.

Each layer of the tracker provides an independent measurement of charge Z with a resolution of $\sigma_Z = 0.092$ charge units for $|Z|$=1 particles. Overall, the inner tracker has a resolution of $\sigma_Z = 0.049$ charge units for $|Z|$=1 particles.

As seen from Fig. S1, two of the TOF planes are located above the magnet (upper TOF) and two planes are below the magnet (lower TOF). The overall velocity ($\beta = v/c$) resolution has been measured to be $\sigma(1/\beta) = 0.04$ for $|Z|$=1 particles. This discriminates between upward- and downward-going particles. The pulse heights of the two upper planes are combined to provide an independent measurement of the charge with an accuracy $\sigma_Z = 0.06$ charge units for $|Z|$=1 particles. The pulse heights from the two lower planes are combined to provide another independent charge measurement with the same accuracy.

Electrons traversing AMS were triggered as described in Ref. [8]. Figure S2 shows the evolution of the electron trigger efficiency as a function of time.

Monte Carlo (MC) simulated events were produced using a dedicated program developed by the collaboration based on the GEANT4-10.3 package [42]. The program simulates electromagnetic and hadronic [43] interactions of particles in the material of AMS and generates detector responses. The digitization of the signals is simulated precisely according to the measured characteristics of the electronics. The simulated events then undergo the same reconstruction as used for the data.

Event Selection.—AMS has collected 1.9×10^{11} cosmic ray events from May 20, 2011 to November 2, 2021. The collection time used includes only those seconds during which the detector was in normal operating conditions and, in addition, AMS was pointing within 40° of the local zenith and the ISS was outside of the South Atlantic Anomaly. Because of the geomagnetic field, the daily collection time of the electron fluxes is (1.6 – 3.7) $\times 10^3$ s at 1 GV, (4.5 – 7.5) $\times 10^3$ s at 2 GV, (1.8 – 2.3) $\times 10^4$ s at 5 GV, (3.3 – 3.8) $\times 10^4$ s at 10 GV, (6.1 – 7.0) $\times 10^4$ s at 20 GV, and, above 30 GV, reaches (6.7 – 7.3) $\times 10^4$ s out of 8.64 $\times 10^4$ s per day.

The event selection is designed to minimize the total error. Electron events are required to be downward going (TOF $\beta > 0.8$) and to have a reconstructed track in the inner tracker. Tracking fitting quality criteria such as $\chi^2 < 20$ in both bending and no-bending plane are applied to ensure good accuracy of the track reconstruction. The charge measurements in TOF and tracker are required to be compatible with $|Z|$=1. The evolution of the selection efficiency as a function of time is shown in Fig. S3.

The measured rigidity is required to be greater than the local geomagnetic cutoff. The local geomagnetic cutoff was calculated as the maximum geomagnetic cutoff within the AMS field of view from AMS data by measuring the electron flux at each geomagnetic position. The details of this study will be included in a future publication [44]. To estimate the associated systematic error, we increase the calculated value of the geomagnetic cutoff by 10%. This results in a systematic error on the fluxes of $< 2\%$ at 1 GV and negligible ($< 0.4\%$) above 2 GV. We have verified that using a geomagnetic cutoff derived from the most recent International Geomagnetic Reference Field (IGRF) model [45] with external non-symmetric magnetic fields [46] during the most geomagnetically disturbed periods does not introduce observable changes in the flux values nor in the systematic errors.

The small corrections δ_i^j are estimated on daily basis by comparing the efficiencies in data and Monte Carlo simulation of every selection cut using information from the detectors unrelated to that cut. The estimated δ_i^j values are smoothed as a function of time and their scatter is taken as the associated systematic error on the electron flux.

Event satisfying the selection criteria are classified into two categories: positive and negative rigidity data samples. In this Letter we only consider the negative rigidity data sample, which comprises mostly electrons, antiprotons, and a small amount of light negative mesons (π^- and a negligible amount of K^-) produced in the interactions of primary cosmic rays with the detector materials, and charge confusion protons and positrons reconstructed in the tracker with negative rigidity due to the finite tracker resolution or due to interactions with the detector materials.

The TRD estimator Λ_{TRD} is constructed from the ratio of the log–likelihood probability of the $e^\pm$ hypothesis to that of the p hypothesis in each layer of TRD [8]. Electrons and positrons, which have $\Lambda_{TRD} \sim 0.4$, are efficiently separated from antiprotons (and protons), which have $\Lambda_{TRD} \sim 1$.

The number of electrons and its statistical error in each rigidity and time bin are determined by fitting signal and background Λ_{TRD} templates to data by varying their respective normalizations. Figure S4 shows the fit result for four rigidity bins from 1.00 to 11.0 GV of June 1, 2011.

The amount of charge confused positron is estimated from MC simulation and subtracted from the number of electron. The accuracy of $e^\pm$ MC simulation are verified by the events passing though ECAL [8]. The charge confusion positron are negligible ($< 0.1\%$) in all the rigidity bin below 41.9 GV .

In total 2.0×10^8 electrons are identified in the energy range from 1.0 GeV to 41.9 GV.

Daily electron fluxes are also measured with traditional analysis within ECAL acceptance and, for this case, the particle energy is determined with ECAL [17,18]. Figure S5 shows the comparison of the daily electron fluxes from these two methods for four rigidity bins from 1.00 to 11.0 GV. As seen, the results are consistent. The analysis of the events with TRD provides statistically significant improvement of the data below 41.9 GV without effects on the systematic errors.

TABLE SA. The range of each year from 2011 to 2021 in BRs and dates.

Year	Range [BR]	Range [Date]
2011	2426 – 2433	May 20, 2011 – December 16, 2011
2012	2434 – 2447	December 17, 2011 – December 28, 2012
2013	2448 – 2461	December 29, 2012 – January 10, 2014
2014	2462 – 2471	January 11, 2014 – September 29, 2014
2015	2473 – 2488	November 29, 2014 – January 9, 2016
2016	2489 – 2502	January 10, 2016 – January 21, 2017
2017	2503 – 2515	January 22, 2017 – January 7, 2018
2018	2516 – 2528	January 8, 2018 – December 24, 2018
2019	2529 – 2540	December 25, 2018 – October 29, 2019
2020	2543 – 2554	January 26, 2020 – November 18, 2020
2021	2554 – 2567	November 19, 2020 – November 2, 2021

Wavelet Analysis.—The continuous wavelet transform W_n of a time series x_n with equal time interval δt is defined as [61]:

$$W_n(s) = \sum_{n'=1}^{N} x_{n'} \psi^* \left[\frac{(n'-n)\delta t}{s} \right], \tag{S1}$$

where the $*$ indicates the complex conjugate of the wavelet function ψ, s is the period, and n is the time index of the wavelet. In this study, we chose the Morlet wavelet, consisting of a plane wave modulated by a Gaussian:

$$\psi(\eta) = \pi^{-1/4} e^{i6\eta} e^{-\eta^2/2}, \tag{S2}$$

where η is a nondimensional time parameter. The wavelet power is given by $|W_n(s)|^2$. The wavelet time-frequency power spectrum shows the temporal distribution of the power for each period s. The time-averaged power spectrum over a certain time interval is

$$\overline{W}_n^2(s) = \frac{1}{n_2 - n_1 + 1} \sum_{n=n_1}^{n_2} |W_n(s)|^2, \tag{S3}$$

where n_1 and n_2 are the beginning and ending indexes of the analyzed time interval, respectively.

In both the wavelet time-frequency power spectrum and time-averaged power spectrum, the normalized power is defined by the wavelet power divided by the variance σ^2 of the time series x_n in the corresponding time interval:

$$\sigma^2 = \frac{\sum_{n=n_1}^{n_2} (x_n - \overline{x})^2}{n_2 - n_1}, \tag{S4}$$

where $\overline{x}$ is the mean value of the time series. This normalization by variance is applied to show the strength of the periodicities.

To determine significance levels above which the power represents periodic structures, Monte Carlo simulations are used to assess the statistical significance against backgrounds which are generated by the lag-1 autoregressive process [61]:

$$y_n = \alpha y_{n-1} + z_n, \tag{S5}$$

where z_n is a Gaussian with zero mean and width such that the variance of the simulated time series is equal to the measured time series. Here, α is the lag-1 autocorrection obtained from the measured time series x_n:

$$\alpha = \frac{\sum_{n=1}^{N-1} (x_n - \overline{x})(x_{n+1} - \overline{x})}{\sum_{n=1}^{N} (x_n - \overline{x})^2}, \tag{S6}$$

where N is the number of measured points and $\overline{x}$ is the mean value of the time series.

For each period, the 95% confidence level is determined by the power exceeded by 5% of the power values calculated from the simulated background. The 95% confidence level has different shapes due to different solar modulation effects as a function of rigidity.

Hysteresis Analysis.—The hysteresis occurs over the time span from 2011 to 2018 as seen in Fig. S25 and Fig. 3. To analyze the significance of the hysteresis, using a similar method as Ref. [31], we select the two time intervals with the same Φ_{e^-}, one before 2014-2015 and one after, with the most significant difference in Φ_p. This minimizes the systematic errors such as the error from unfolding. From this, we determine that the maximum difference for [1.00–1.71] GV is at $\Phi_{e^-} = 14.27$ m^{-2}sr^{-1}s^{-1}GV^{-1} which occurs in 2012 (A) and 2016 (B). The variation in Φ_p is $\Phi_p^B/\Phi_p^A = 1.707 \pm 0.027$, see Fig. S25(a). The errors in both Φ_p and Φ_{e^-} are accounted for in the error calculation of the ratio. To obtain the overall significance of the hysteresis, we repeat the procedure for remaining non-overlapping time intervals and determine that the maximum difference for [1.00–1.71] GV is at $\Phi_{e^-} = 20.21$ m^{-2}sr^{-1}s^{-1}GV^{-1} which occurs in 2011 (C) and 2018 (D). The variation in proton flux is $\Phi_p^D/\Phi_p^C = 1.656 \pm 0.025$. The analysis is repeated for other rigidity bins, see Fig. S25(b - i).

Figure S26 shows the proton flux ratios Φ_p^B/Φ_p^A and Φ_p^D/Φ_p^C as a function of rigidity. As seen, the difference in Φ_p decreases with increasing rigidity. In particular, at [7.09–8.48] GV, with $\Phi_p^B/\Phi_p^A = 1.074 \pm 0.016$ and $\Phi_p^D/\Phi_p^C = 1.062 \pm 0.016$, the combined significance of the difference in Φ_p before and after 2014-2015 is 6.1σ. At [8.48 – 11.0] GV, with $\Phi_p^B/\Phi_p^A = 1.048 \pm 0.016$ and $\Phi_p^D/\Phi_p^C = 1.042 \pm 0.016$, the combined significance of the difference in Φ_p before and after 2014-2015 is 4.1σ.

In summary, the hysteresis is observed with a significance greater than 6σ below 8.48 GV and with 4.1σ at [8.48 – 11.0] GV.

Hysteresis Structures Analysis.— The hysteresis exhibits structures during the flux dips in 2015 and 2017, see Figs. 4 and S27 for the rigidity bin [1.00–1.71] GV. To analyze the significance of the hysteresis structures in 2015, we select the two time intervals with the same Φ_p one in the first half (E) and one in the second half (F) of region IV, with the most significant difference in Φ_{e^-}. From this, we determine that the maximum difference for [1.00–1.71] GV is at $\Phi_p = 466.5$ m^{-2}sr^{-1}s^{-1}GV^{-1}, the variation in Φ_{e^-} is $\Phi_{e^-}^F/\Phi_{e^-}^E = 0.827 \pm 0.013$, see Fig. S27(c). The errors in both Φ_{e^-} and Φ_p are accounted for in the error calculation of the ratio. To obtain the overall significance of the hysteresis structure, we repeat the procedure for remaining non-overlapping time intervals of region IV and determine that the maximum difference for [1.00–1.71] GV is at $\Phi_p = 552.1$ m^{-2}sr^{-1}s^{-1}GV^{-1}, indicated as G and H in Fig. S27(c). The variation in electron flux is $\Phi_{e^-}^H/\Phi_{e^-}^G = 0.831 \pm 0.014$. Both $\Phi_{e^-}^F/\Phi_{e^-}^E$ and $\Phi_{e^-}^H/\Phi_{e^-}^G$ deviate from unity. The overall significance of the hysteresis structure corresponding to the dip in 2015 is 15.9σ. The analysis is repeated for the dip in 2017 (V), as shown in Fig. S27(d), with the four corresponding points J, K, L, M. The variation in Φ_{e^-} is $\Phi_{e^-}^J/\Phi_{e^-}^K = 0.935 \pm 0.015$ for $\Phi_p = 1089.7$ m^{-2}sr^{-1}s^{-1}GV^{-1}, and $\Phi_{e^-}^L/\Phi_{e^-}^M = 0.914 \pm 0.015$ for $\Phi_p = 1224.7$ m^{-2}sr^{-1}s^{-1}GV^{-1}. The significance of the corresponding hysteresis structure is 7.0σ.

The same analysis at the next rigidity bin [1.71 – 2.97] GV is presented in Fig. S28. To analyze the significance of the hysteresis structures in 2015, we select the two time intervals with the same Φ_p one in the first half (E) and one in the second half (F) of region IV, with the most significant difference in Φ_{e^-}. From this, we determine that the maximum difference for [1.71 – 2.97] GV is at $\Phi_p = 346.8$ m^{-2}sr^{-1}s^{-1}GV^{-1}, the variation in Φ_{e^-} is $\Phi_{e^-}^F/\Phi_{e^-}^E = 0.831 \pm 0.013$, see Fig. S28(c). The errors in both Φ_{e^-} and Φ_p are accounted for in the error calculation of the ratio. To obtain the overall significance of the hysteresis structure, we repeat the procedure for remaining non-overlapping time intervals of region IV and determine that the maximum difference for [1.71 – 2.97] GV is at $\Phi_p = 388.2$ m^{-2}sr^{-1}s^{-1}GV^{-1}, indicated as G and H in Fig. S28(c). The variation in electron flux is $\Phi_{e^-}^H/\Phi_{e^-}^G = 0.876 \pm 0.014$. Both $\Phi_{e^-}^F/\Phi_{e^-}^E$ and $\Phi_{e^-}^H/\Phi_{e^-}^G$ deviate from unity. The overall significance of the hysteresis structure corresponding to the dip in 2015 is 14.6σ.

The analysis is repeated for the dip in 2017 (V), as shown in Fig. S28(d), with the four corresponding points J, K, L, M. The variation in Φ_{e^-} is $\Phi_{e^-}^{J}/\Phi_{e^-}^{K} = 0.942 \pm 0.015$ for $\Phi_p = 603.2\ \mathrm{m^{-2}sr^{-1}s^{-1}GV^{-1}}$, and $\Phi_{e^-}^{L}/\Phi_{e^-}^{M} = 0.947 \pm 0.015$ for $\Phi_p = 644.1\ \mathrm{m^{-2}sr^{-1}s^{-1}GV^{-1}}$. The significance of the corresponding hysteresis structure is 5.3σ.

We use two slightly different methods to assess the significance of the hysteresis and of the structures in the hysteresis. They both use two independent pairs of points on the hysteresis curve, namely comparing the difference in electron flux at the same proton flux value (method I), or comparing the difference in proton flux at the same electron flux value (method II).

To analyze the structures in the hysteresis, we used both methods and they show consistent results. Two examples: for the time interval V (flux dip in 2017) and rigidity interval [1.00 - 1.71] GV, the significance of the structure in hysteresis is 7.0σ with method I and 6.9σ with method II. For the time interval V and rigidity interval [1.71 - 2.97] GV, the significance of the structure in hysteresis is 5.3σ with method I and 4.8σ with method II.

We present the results of method I for the analysis of the hysteresis structures and of method II for the analysis of the hysteresis in this Letter. Alternative choice yields consistent results, and all will be presented in Ref. [63]:

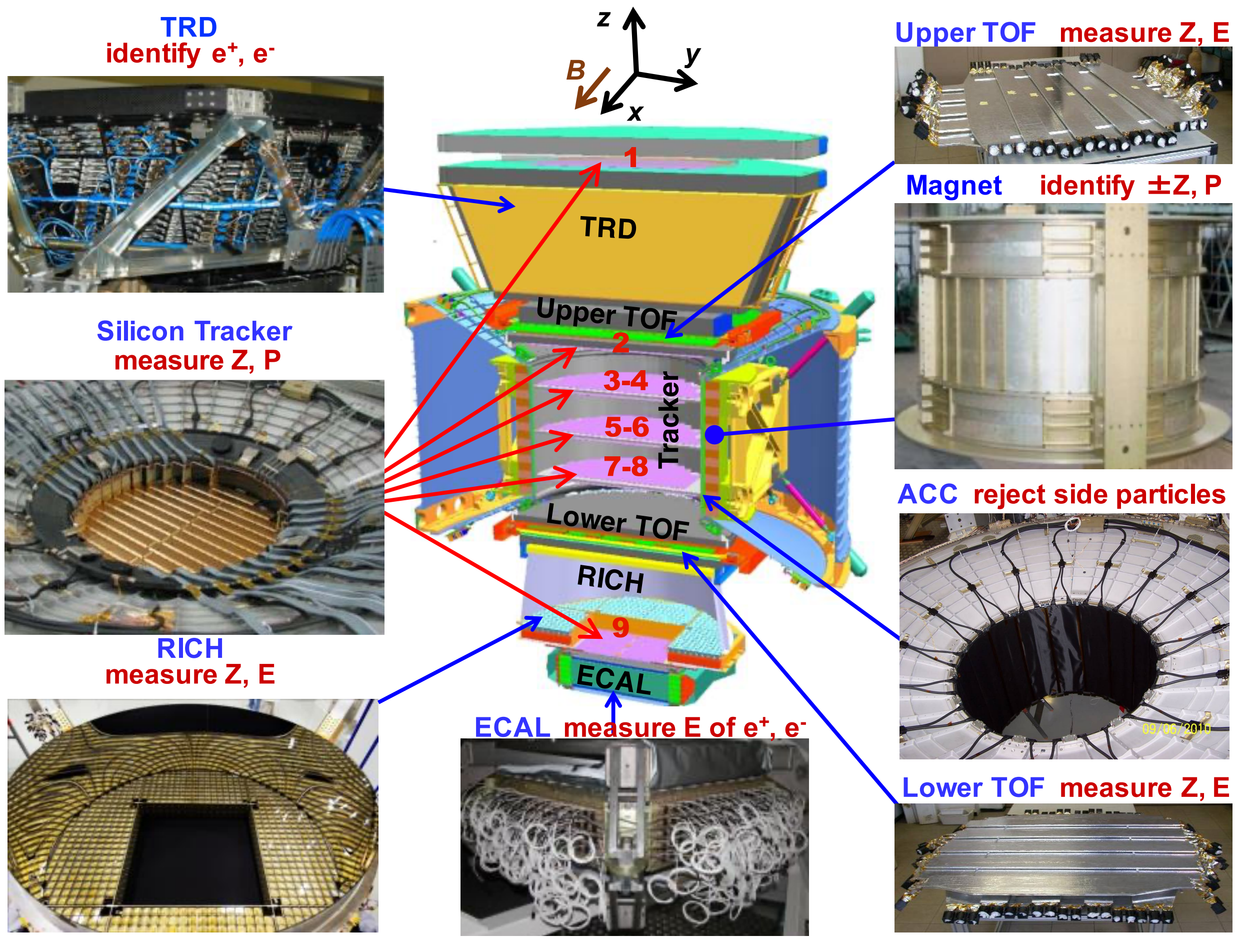

FIG. S1. The AMS detector showing the main elements and their functions. AMS is a TeV precision, multipurpose particle physics magnetic spectrometer in space. It identifies particles and nuclei by their charge Z, energy E, and momentum P or rigidity ($R = P/Z$), which are measured independently by the Tracker, TOF, RICH and ECAL. The ACC counters, located in the magnet bore, are used to reject particles entering AMS from the side. The AMS coordinate system is also shown. The x axis is parallel to the main component of the magnetic field and the z axis points vertically with $z = 0$ at the center of the magnet.

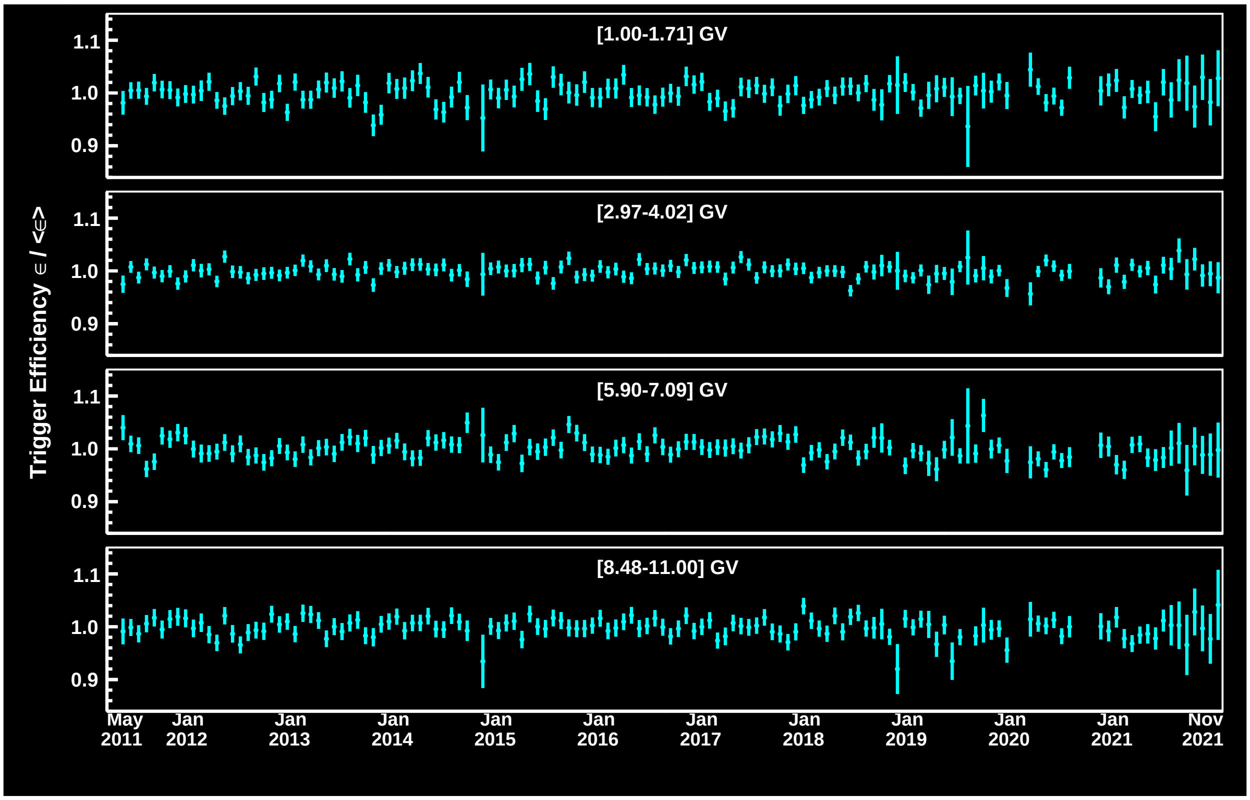

FIG. S2. The evolution of the electron trigger efficiency per Bartels Rotation, ϵ, with respect to its average over the entire time period, $< \epsilon >$, as a function of time for four rigidity bins. Note that, the electron trigger efficiency is measured daily, ϵ is the average over a Bartels Rotation.

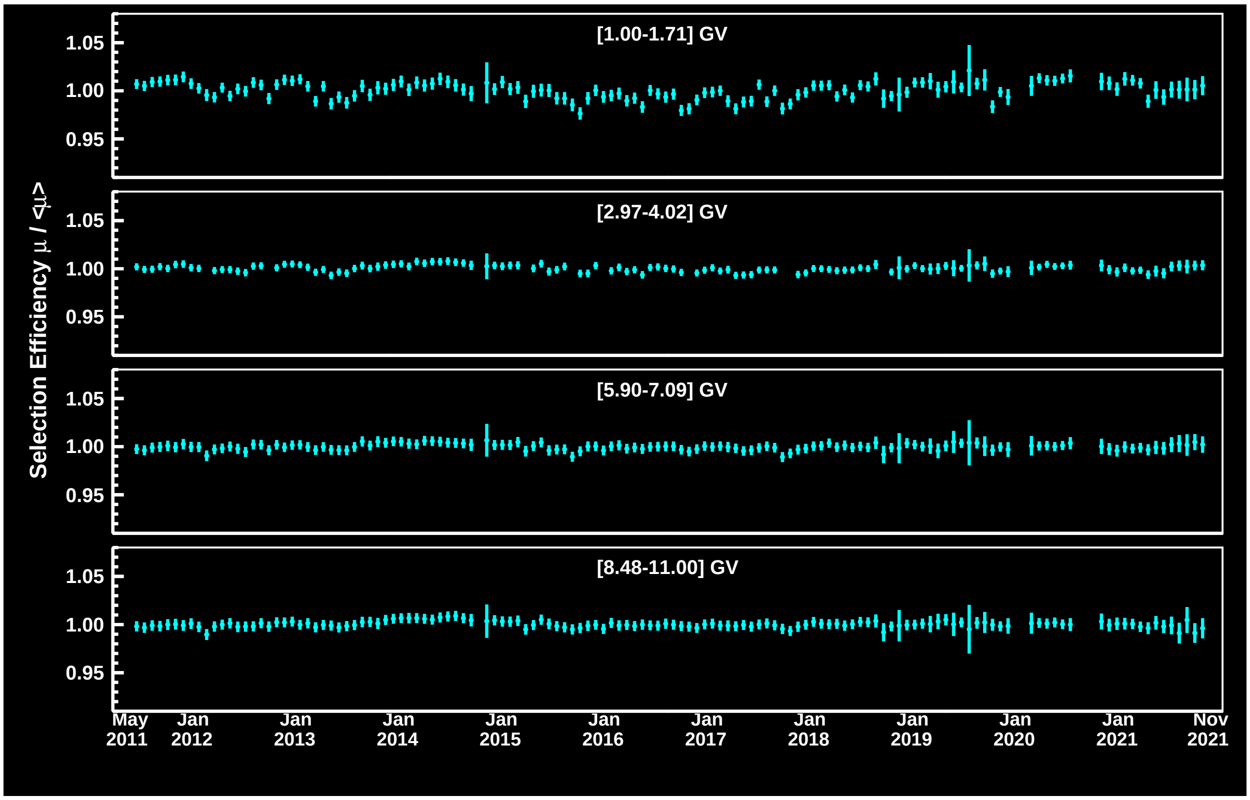

FIG. S3. The evolution of the electron selection efficiency per Bartels Rotation, μ, with respect to its average over the entire time period, $< \mu >$, as a function of time for four rigidity bins. Note that, the electron selection efficiency is measured daily, μ is the average over a Bartels Rotation.

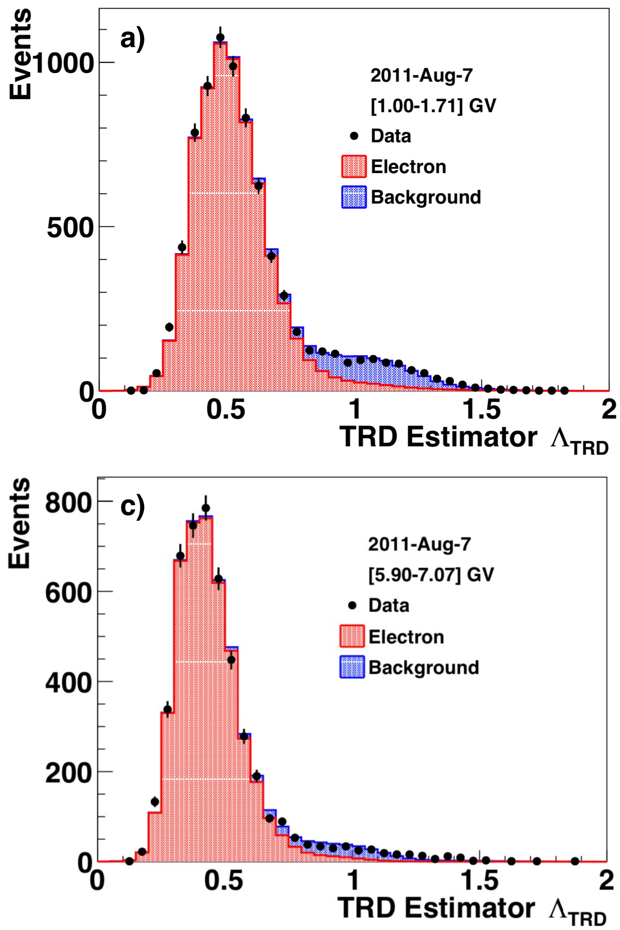

FIG. S4. The examples of the daily data selection in four rigidity bins from 1.00 to 11.0 GV for the negative rigidity sample. The TRD estimator Λ_{TRD} distribution of the selected data events (black data points) is shown together with the electron signal (red shaded area) and backgrounds (blue shaded area). The backgrounds mostly consist of antiprotons and light negative mesons (π^- and a negligible amount of K^-) produced in the interactions of primary cosmic rays with the detector materials. The charge confusion positrons are negligible.

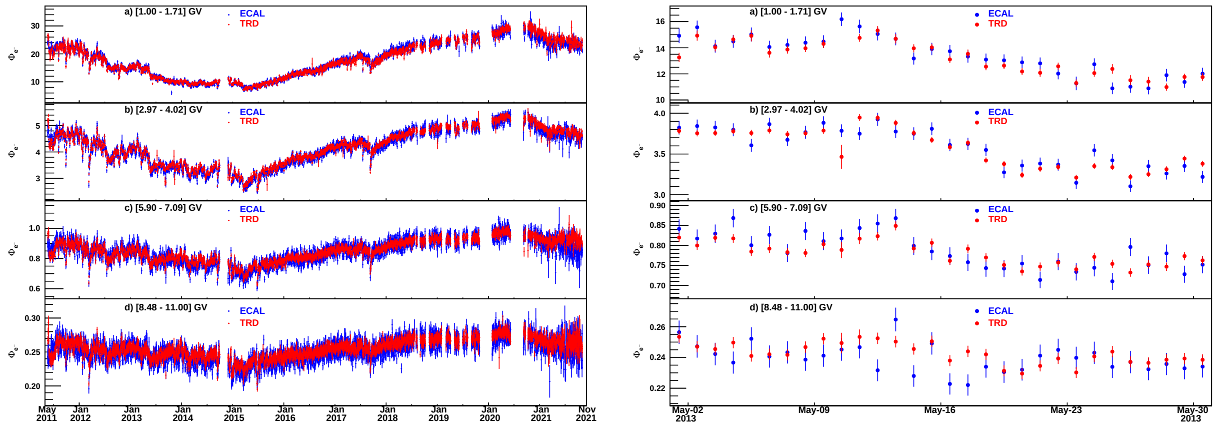

FIG. S5. Comparison of the daily electron fluxes Φ_{e^-} in units of [$\mathrm{m^{-2}sr^{-1}s^{-1}GV^{-1}}$] measured in the TRD acceptance (red data points) and in the ECAL acceptance (blue data points) for four rigidity bins: a) [1.00 - 1.71] GV, b) [2.97 - 4.02] GV, c) [5.90 - 7.09] GV, and d) [8.48 - 11.0] GV. The left figure is the comparison over eleven years. The right figure is an example of the daily comparison for the month of May 2013. The results from the two analysis methods are consistent, and the analysis in the TRD acceptance provides statistically significant improvement of the data without effects on the systematic errors. For the traditional analysis in the ECAL acceptance [17, 18], the particle energy is determined with ECAL.

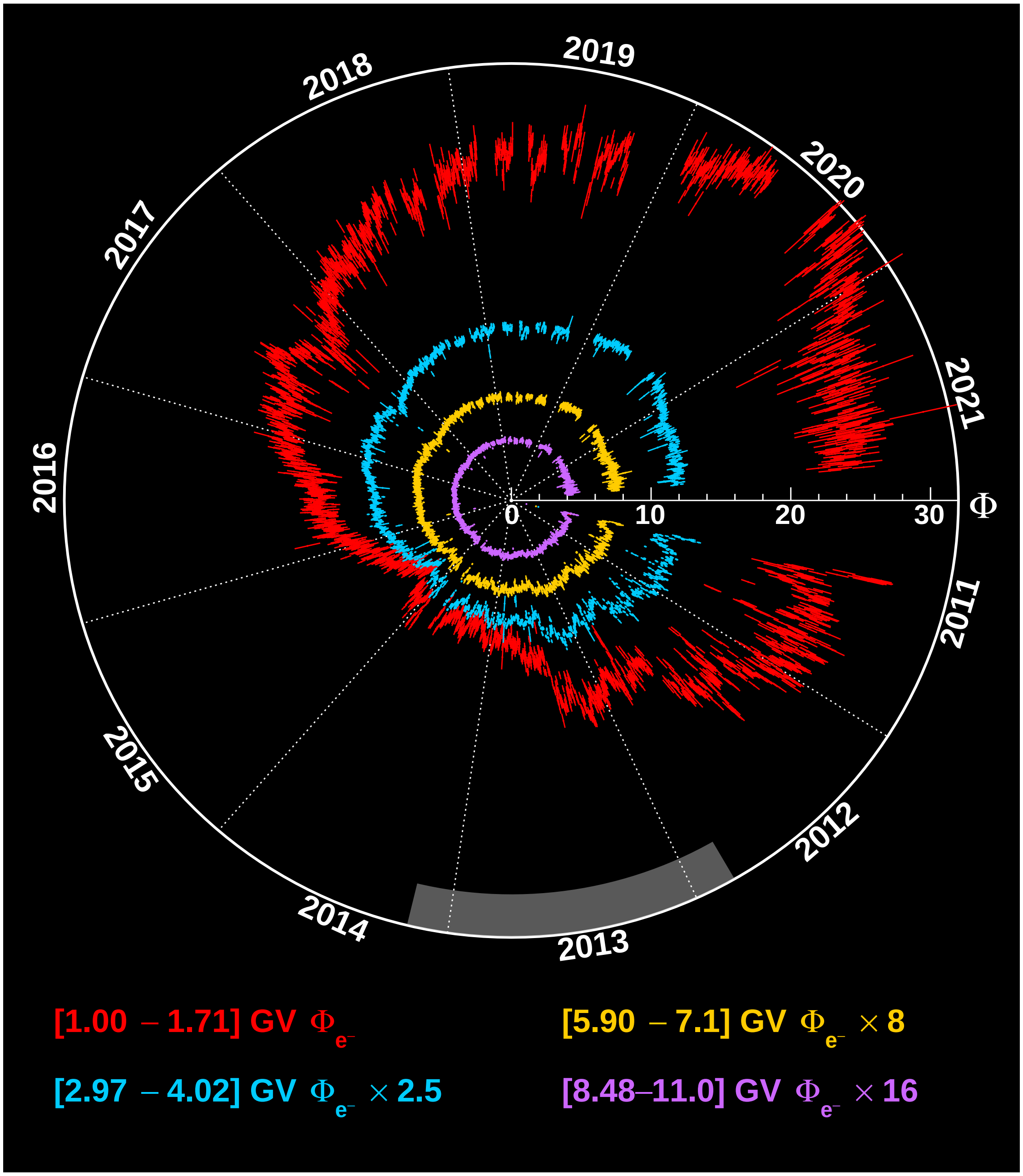

FIG. S6. The eleven-year daily AMS electron fluxes Φ_{e^-} for four rigidity bins from 1.00 to 11.0 GV. The fluxes in units of $[\mathrm{m^{-2}sr^{-1}s^{-1}GV^{-1}}]$ are measured from May 20, 2011 to November 2, 2021, which covers the ascending phase, the maximum, and descending phase to the minimum of solar cycle 24, and part of the ascending phase of solar cycle 25. The gray shaded area in the outer circle corresponds to the time period when the solar magnetic field polarity reversed. The gaps in the fluxes are due to detector studies and upgrades. The scale of the fluxes is shown on the radius. The fluxes are multiplied by different scale factors as indicated. As seen, the electron fluxes exhibit large variations with multiple time scales, and the relative magnitude of these variations decreases with increasing rigidity.

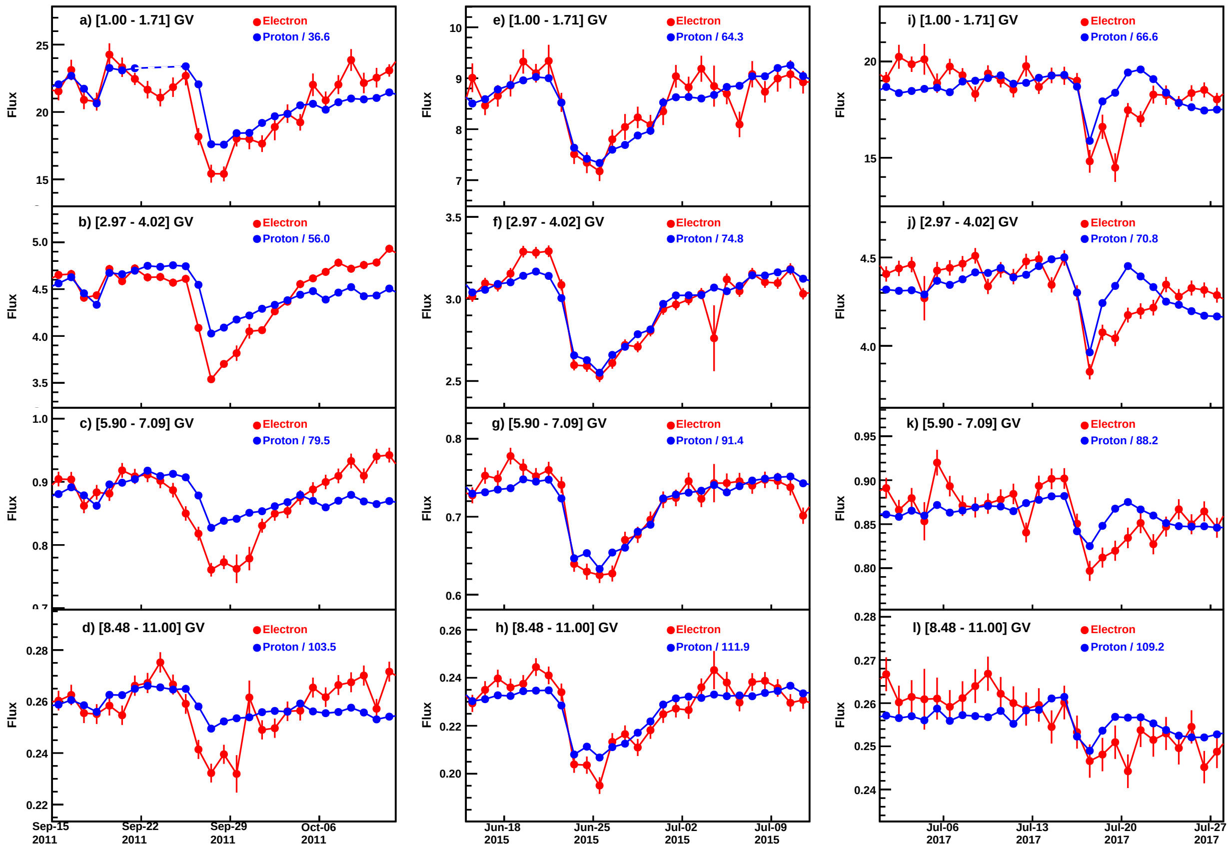

FIG. S7. Daily electron fluxes Φ_{e^-} (red points) and proton fluxes Φ_p (blue points) in units of [$\mathrm{m}^{-2}\mathrm{sr}^{-1}\mathrm{s}^{-1}\mathrm{GV}^{-1}$] during three time intervals: (a, b, c, d) from September 15 to October 12, 2011, (e, f, g, h) from June 15 to July 12, 2015, (i, j, k, l) from July 1 to July 28, 2017. (a, e, i) is for rigidity bin [1.00 – 1.71] GV, (b, f, j) for [2.97 – 4.02] GV, (c, g, k) for [5.90 – 7.09] GV, and (d, h, l) for [8.48 – 11.0] GV. The scale factors of Φ_p, as indicated, are chosen such that Φ_{e^-} and Φ_p are at the same magnitude on average for each rigidity bin and time interval. The contiguous data points are connected with lines to guide the eye. The proton fluxes during a Solar Energetic Particle (SEP) event are not shown and the measurements before and after that SEP event are connected with a dashed line in (a). As seen, during lower solar activity (a, b, c, d) and (i, j, k, l), a difference between the short-term evolution of electrons and protons is observed, while during the solar maximum (e, f, g, h) the difference vanishes. For instance, in (b) and (j), the slope of the recovery after the dip is different between electrons and protons. These observations indicate a charge-sign dependence in nonrecurrent solar modulation.

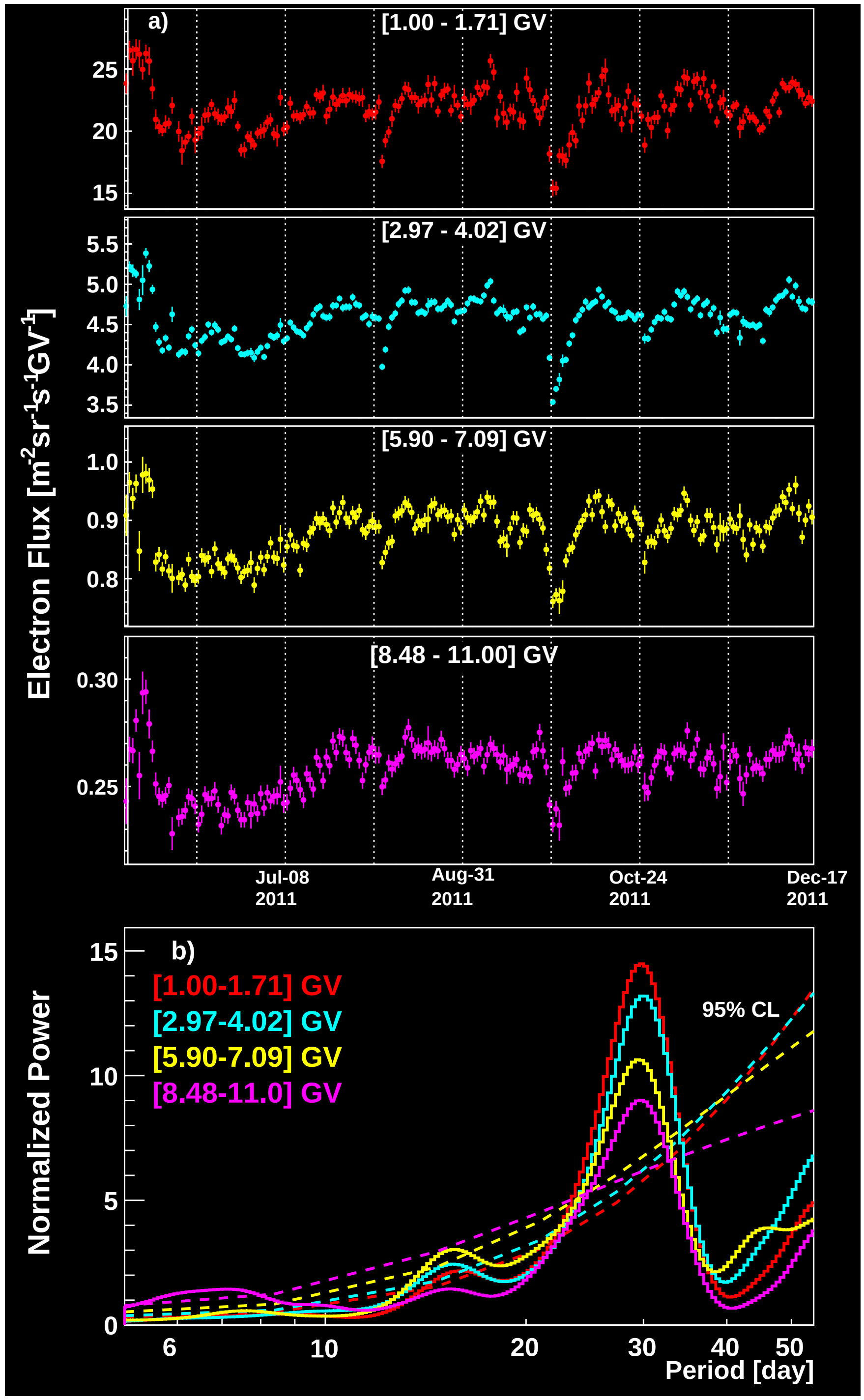

FIG. S8. (a) The daily AMS electron fluxes measured from May 20, 2011 to December 16, 2011 for four rigidity bins. Vertical dashed lines separate Bartels rotations. (b) Wavelet normalized power spectra for the four rigidity bins. Dashed colored curves indicate the 95% confidence levels for the four corresponding rigidity bins.

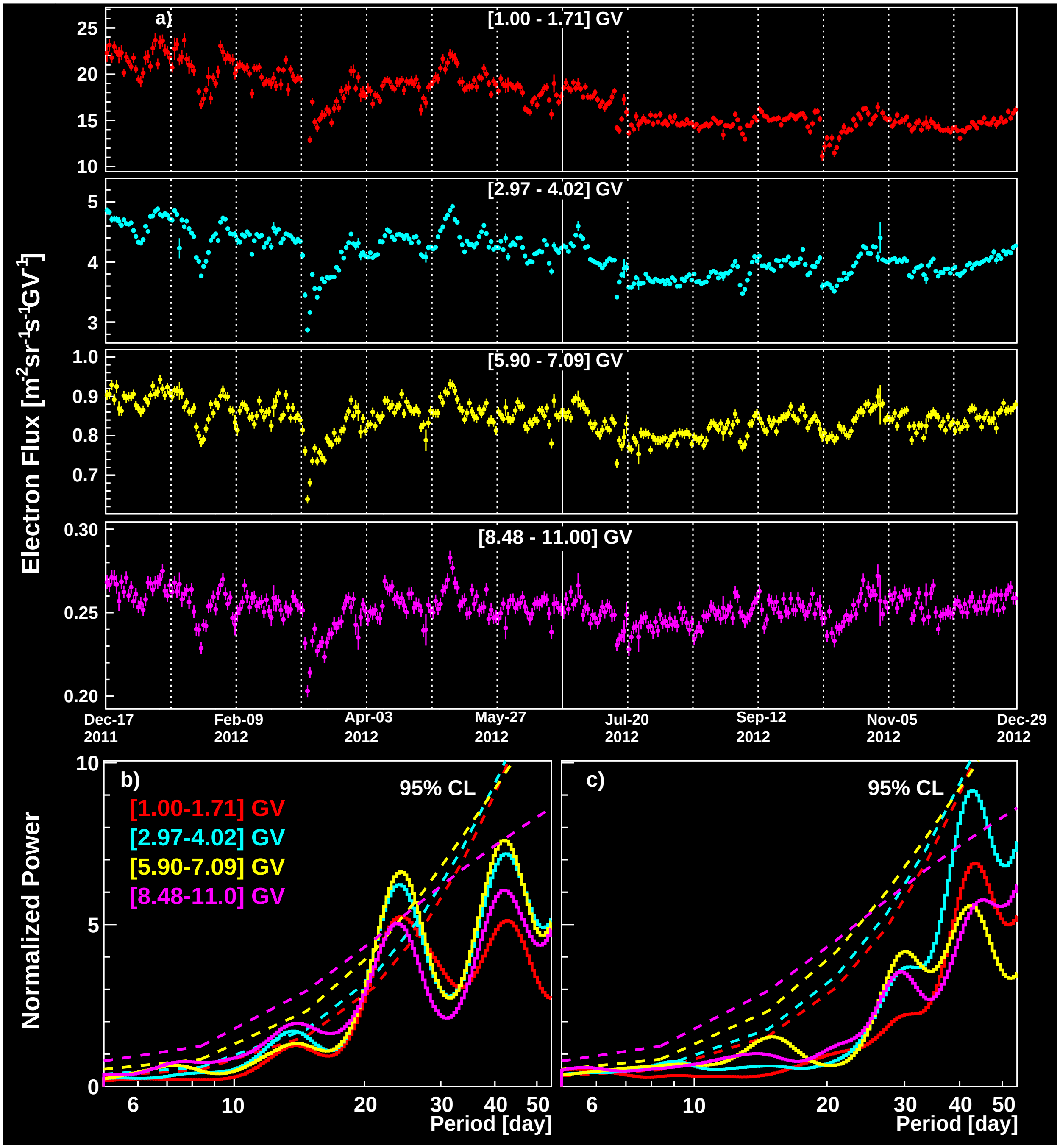

FIG. S9. (a) The daily AMS electron fluxes measured from December 17, 2011 to December 28, 2012 for four rigidity bins. Vertical dashed lines separate Bartels rotations. The vertical solid line separates two equal time intervals where the power spectra are calculated. (b,c) Wavelet normalized power spectra for the four rigidity bins averaged (b) from December 17, 2011 to June 22, 2012 and (c) from June 23, 2012 to December 28, 2012. Dashed colored curves indicate the 95% confidence levels for the four corresponding rigidity bins.

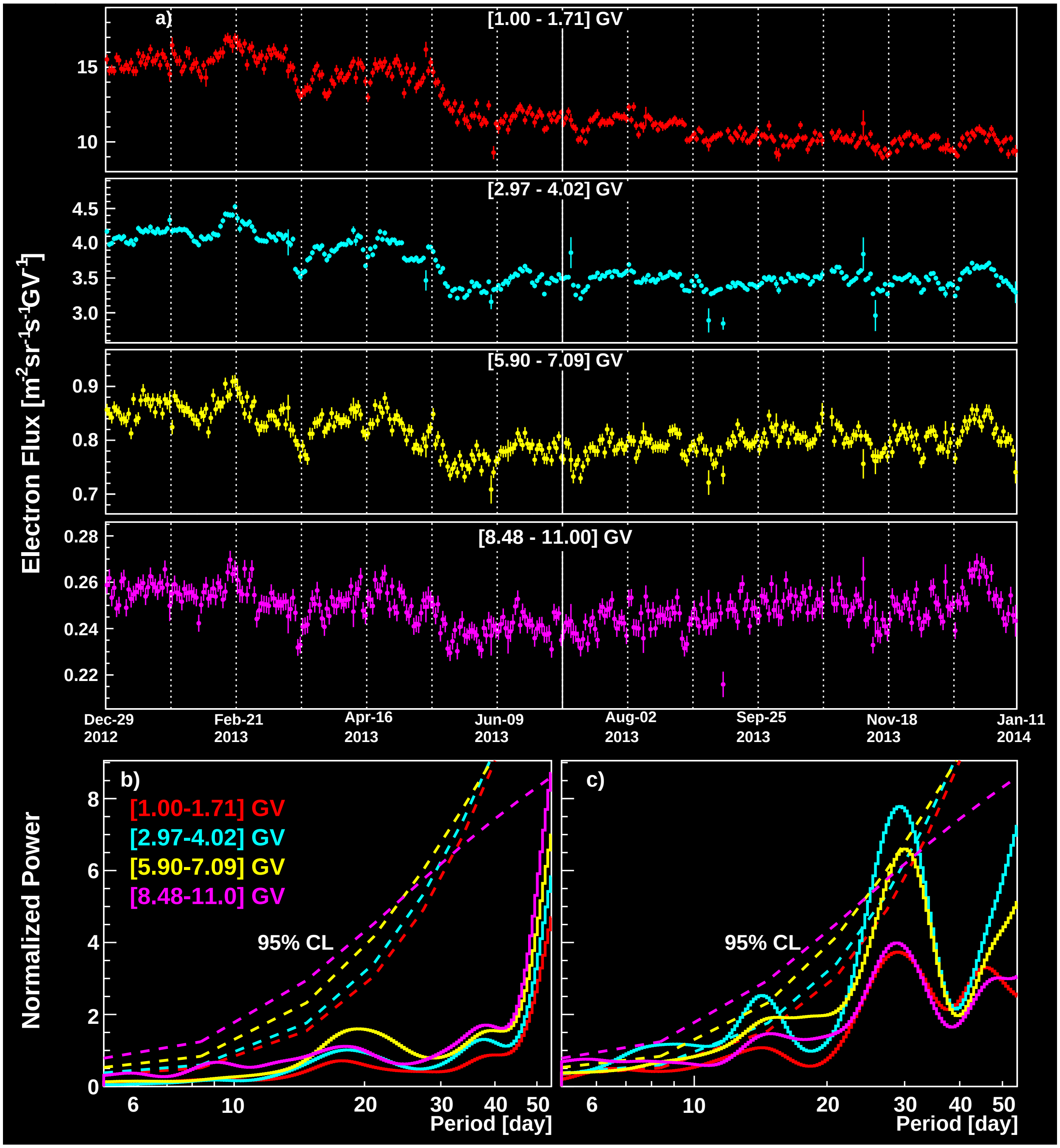

FIG. S10. (a) The daily AMS electron fluxes measured from December 29, 2012 to January 10, 2014 for four rigidity bins. Vertical dashed lines separate Bartels rotations. The vertical solid line separates two equal time intervals where the power spectra are calculated. (b,c) Wavelet normalized power spectra for the four rigidity bins averaged (b) from December 29, 2012 to July 5, 2013 and (c) from July 6, 2013 to January 10, 2014. Dashed colored curves indicate the 95% confidence levels for the four corresponding rigidity bins.

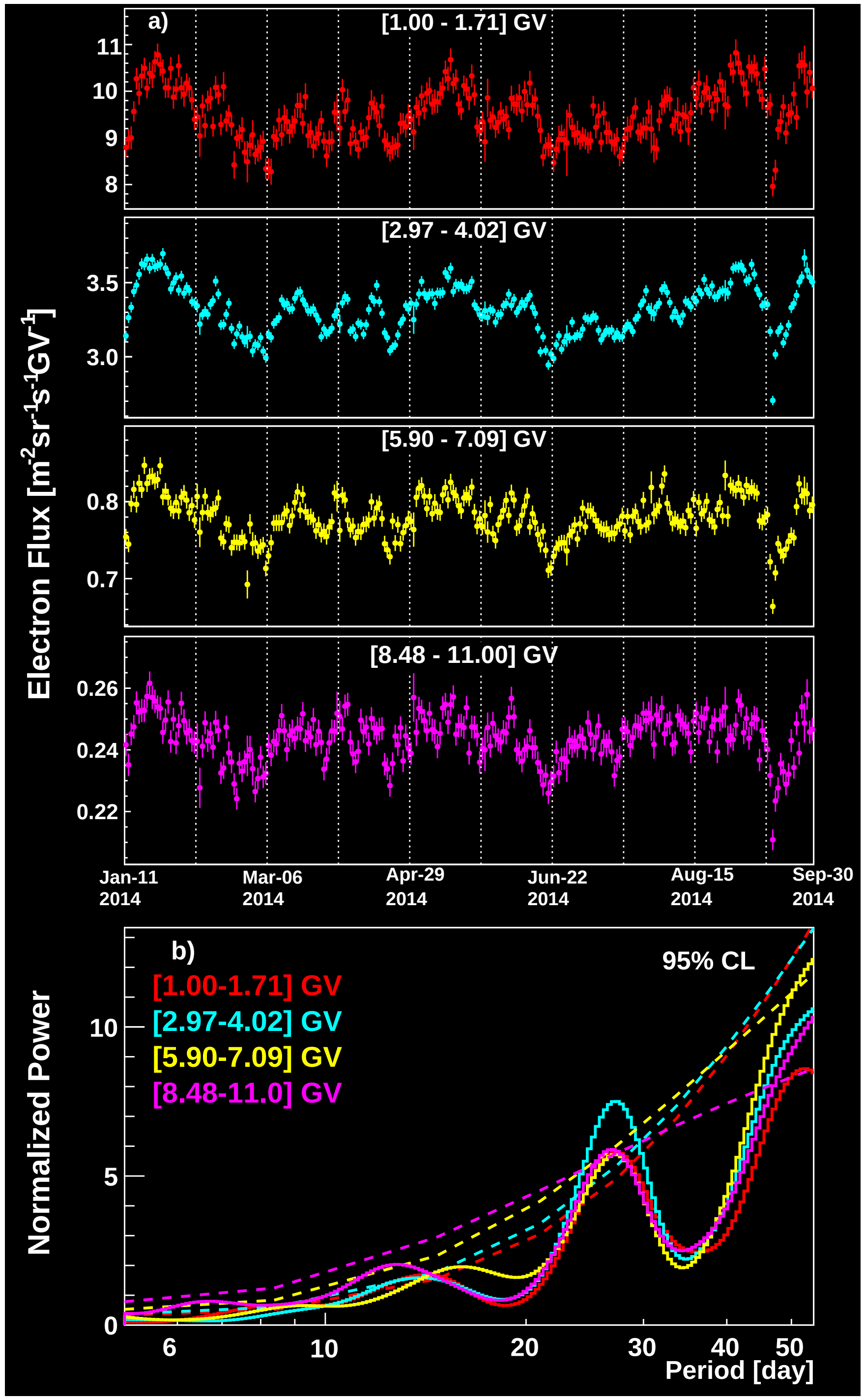

FIG. S11. (a) The daily AMS electron fluxes measured from January 11, 2014 to September 29, 2014 for four rigidity bins. Vertical dashed lines separate Bartels rotations. (b) Wavelet normalized power spectra for the four rigidity bins. Dashed colored curves indicate the 95% confidence levels for the four corresponding rigidity bins. Note that in the time interval from September 30, 2014 to November 28, 2014, AMS was performing detector studies and no data was collected.

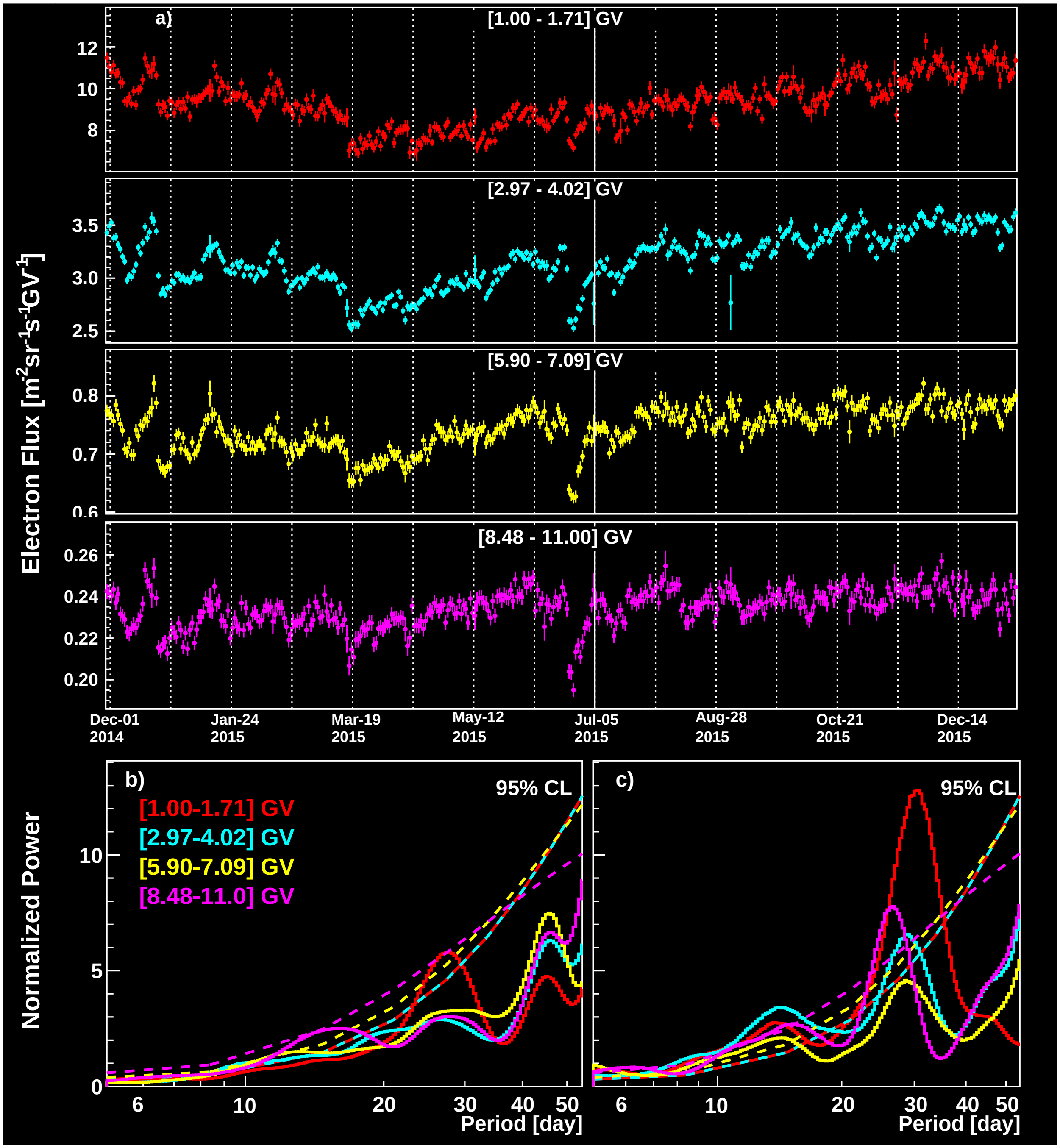

FIG. S12. (a) The daily AMS electron fluxes measured from November 29, 2014 to January 9, 2016 for four rigidity bins. Vertical dashed lines separate Bartels rotations. The vertical solid line separates two approximately equal time intervals where the power spectra are calculated. (b,c) Wavelet normalized power spectra for the four rigidity bins averaged (b) from November 29, 2014 to July 4, 2015 and (c) from July 5, 2015 to January 9, 2016. Dashed colored curves indicate the 95% confidence levels for the four corresponding rigidity bins. Note that portions of the dashed red and dashed cyan curves are close to each other.

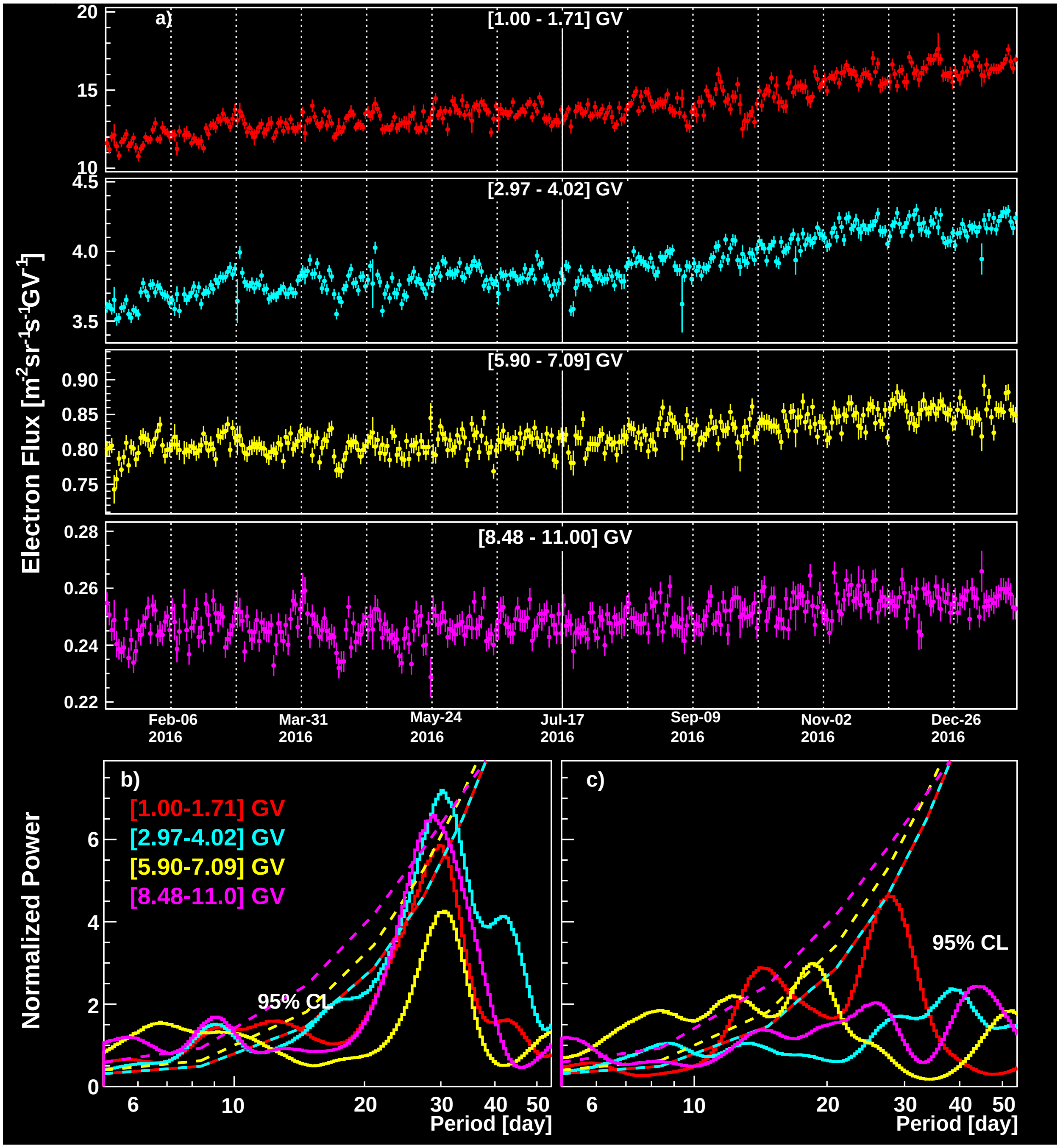

FIG. S13. (a) The daily AMS electron fluxes measured from January 10, 2016 to January 21, 2017 for four rigidity bins. Vertical dashed lines separate Bartels rotations. The vertical solid line separates two equal time intervals where the power spectra are calculated. (b,c) Wavelet normalized power spectra for the four rigidity bins averaged (b) from January 10, 2016 to July 16, 2016 and (c) from July 17, 2016 to January 21, 2017. Dashed colored curves indicate the 95% confidence levels for the four corresponding rigidity bins. Note that portions of the dashed red and dashed cyan curves are close to each other.

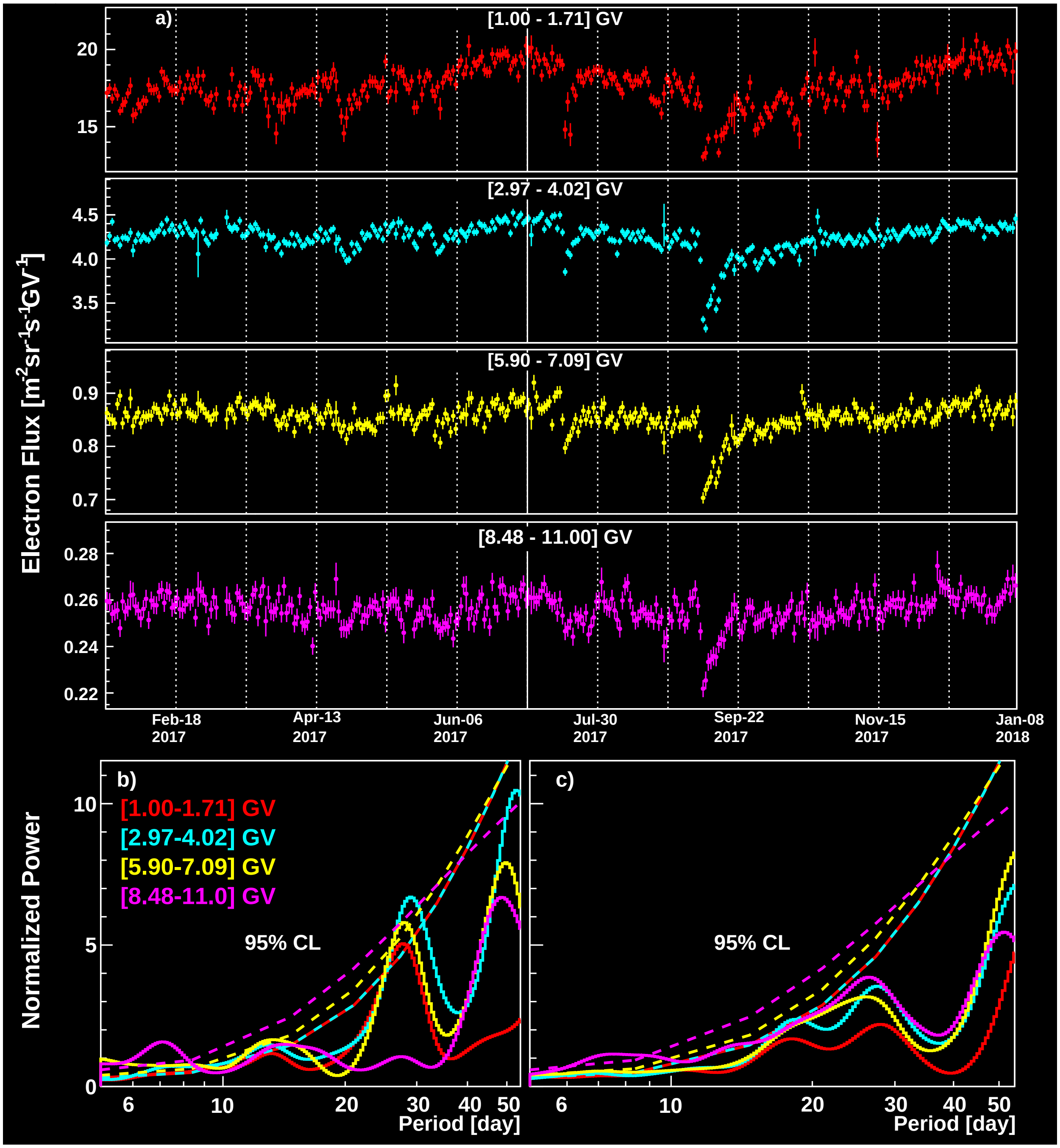

FIG. S14. (a) The daily AMS electron fluxes measured from January 22, 2017 to January 7, 2018 for four rigidity bins. Vertical dashed lines separate Bartels rotations. The vertical solid line separates two approximately equal time intervals where the power spectra are calculated. (b,c) Wavelet normalized power spectra for the four rigidity bins averaged (b) from January 22, 2017 to July 2, 2017 and (c) from July 3, 2017 to January 7, 2018. Dashed colored curves indicate the 95% confidence levels for the four corresponding rigidity bins. Note that portions of the dashed red and dashed cyan curves are close to each other.

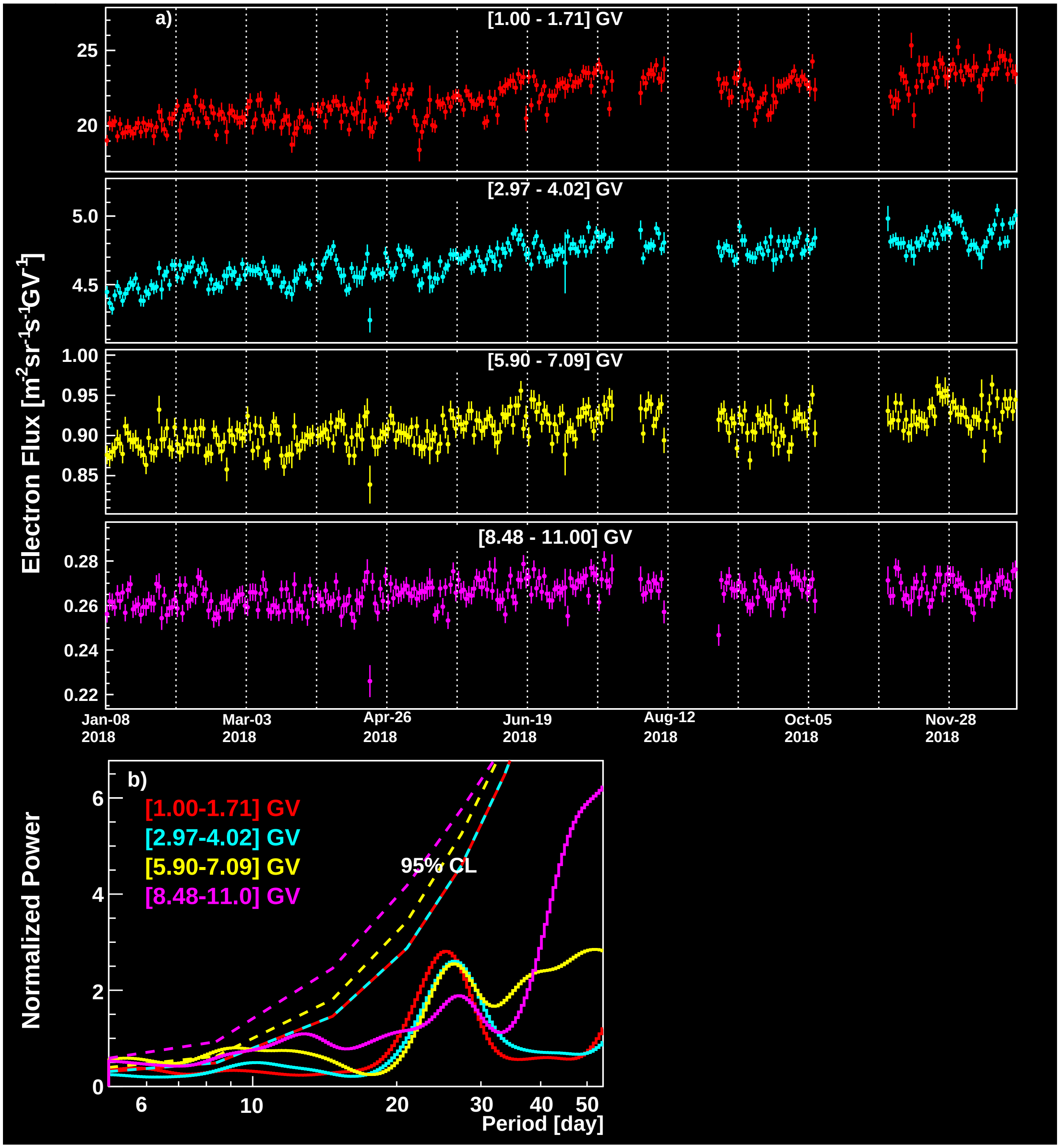

FIG. S15. (a) The daily AMS electron fluxes measured from January 8, 2018 to December 24, 2018 for four rigidity bins. Vertical dashed lines separate Bartels rotations. (b) Wavelet normalized power spectra for the four rigidity bins averaged from January 8, 2018 to July 20, 2018. Dashed colored curves indicate the 95% confidence levels for the four corresponding rigidity bins. Note that portions of the dashed red and dashed cyan curves are close to each other. Due to AMS upgrade, the data after July 20, 2018 is not included in the periodicity analysis.

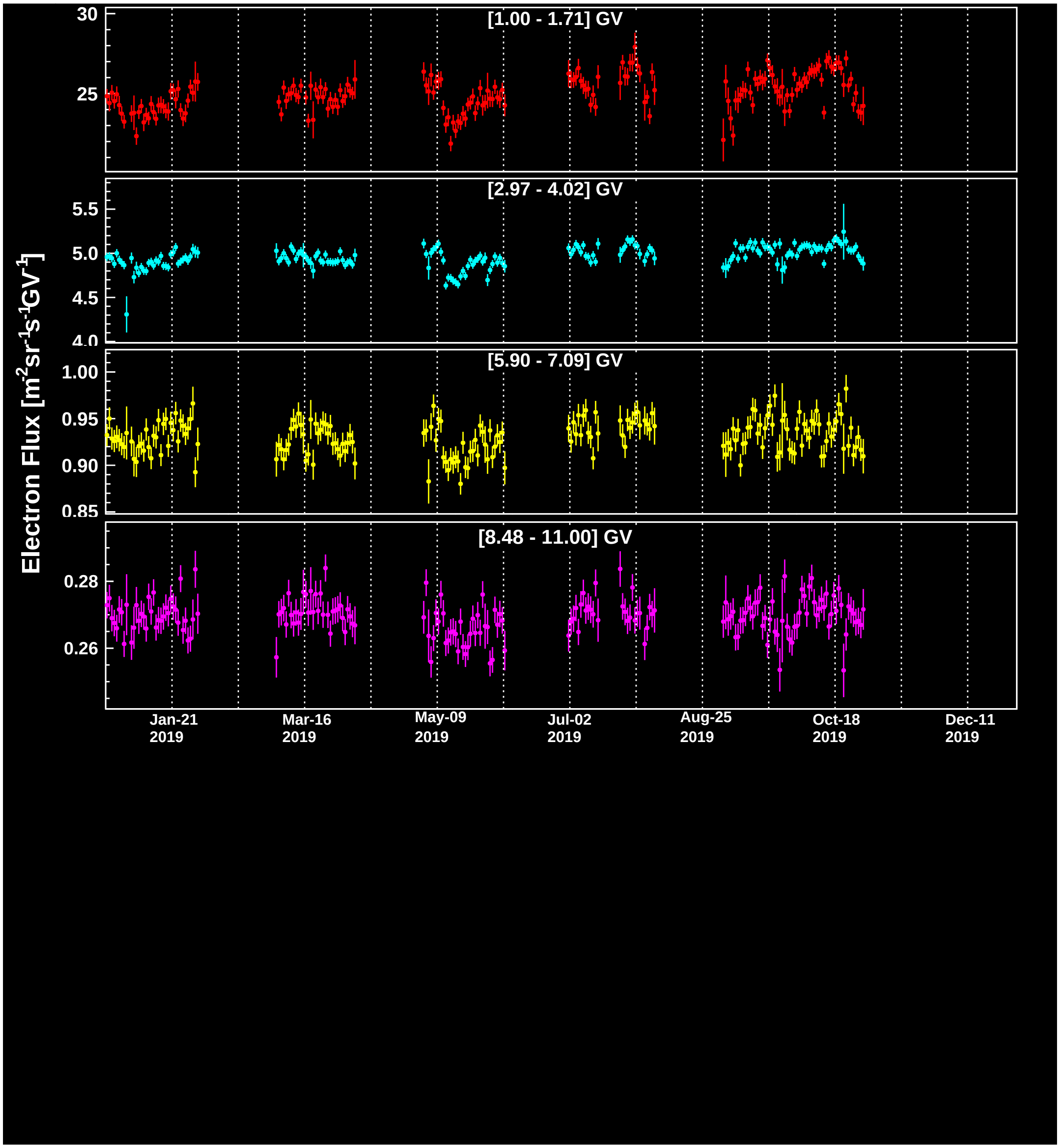

FIG. S16. The daily AMS electron fluxes measured from December 25, 2018 to October 29, 2019 for four rigidity bins. Vertical dashed lines separate Bartels rotations. Due to AMS upgrade, the 2019 data is not included in the periodicity analysis.

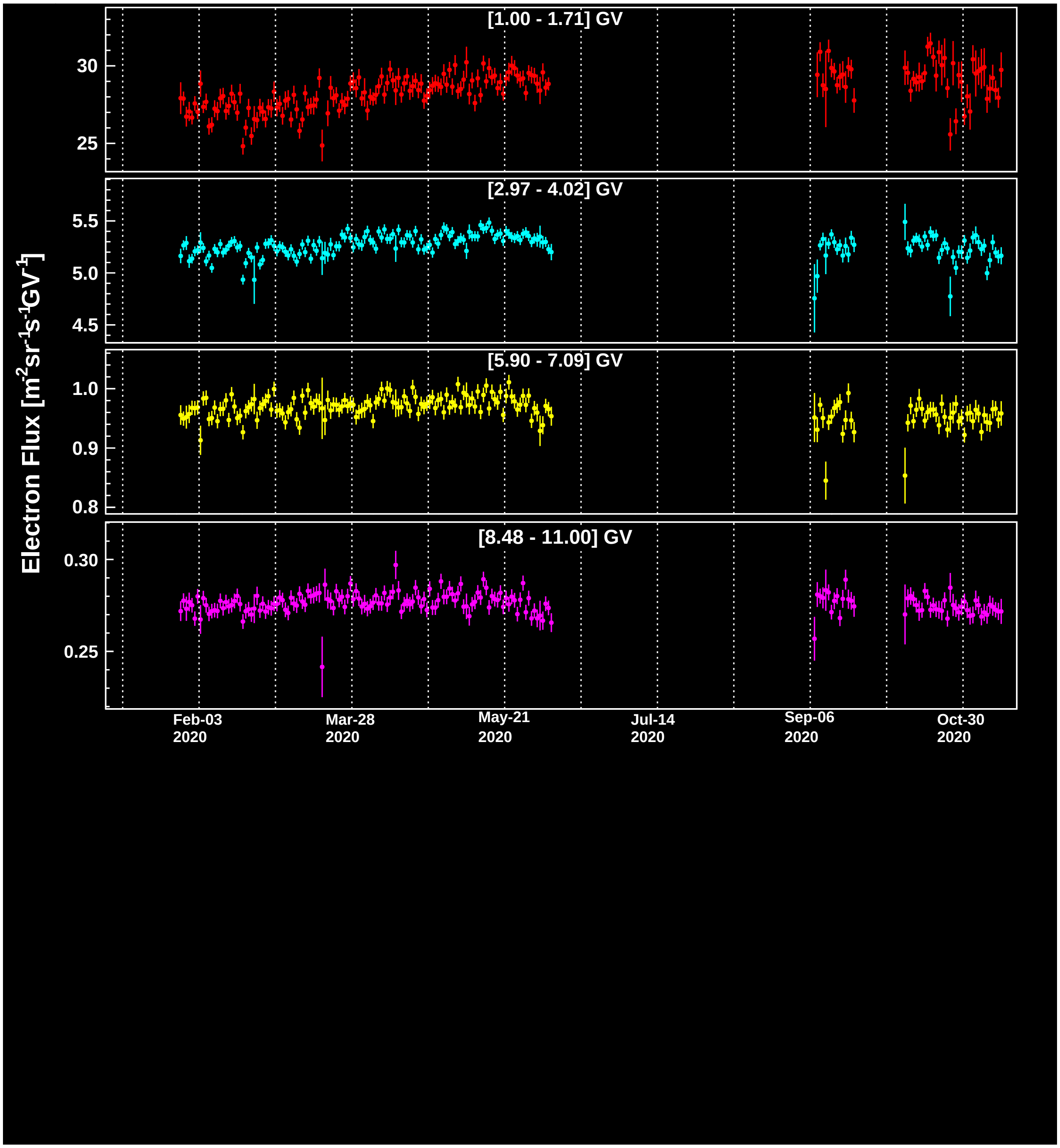

FIG. S17. The daily AMS electron fluxes measured from January 26, 2020 to November 18, 2020 for four rigidity bins. Vertical dashed lines separate Bartels rotations. Due to AMS upgrade, the 2020 data is not included in the periodicity analysis.

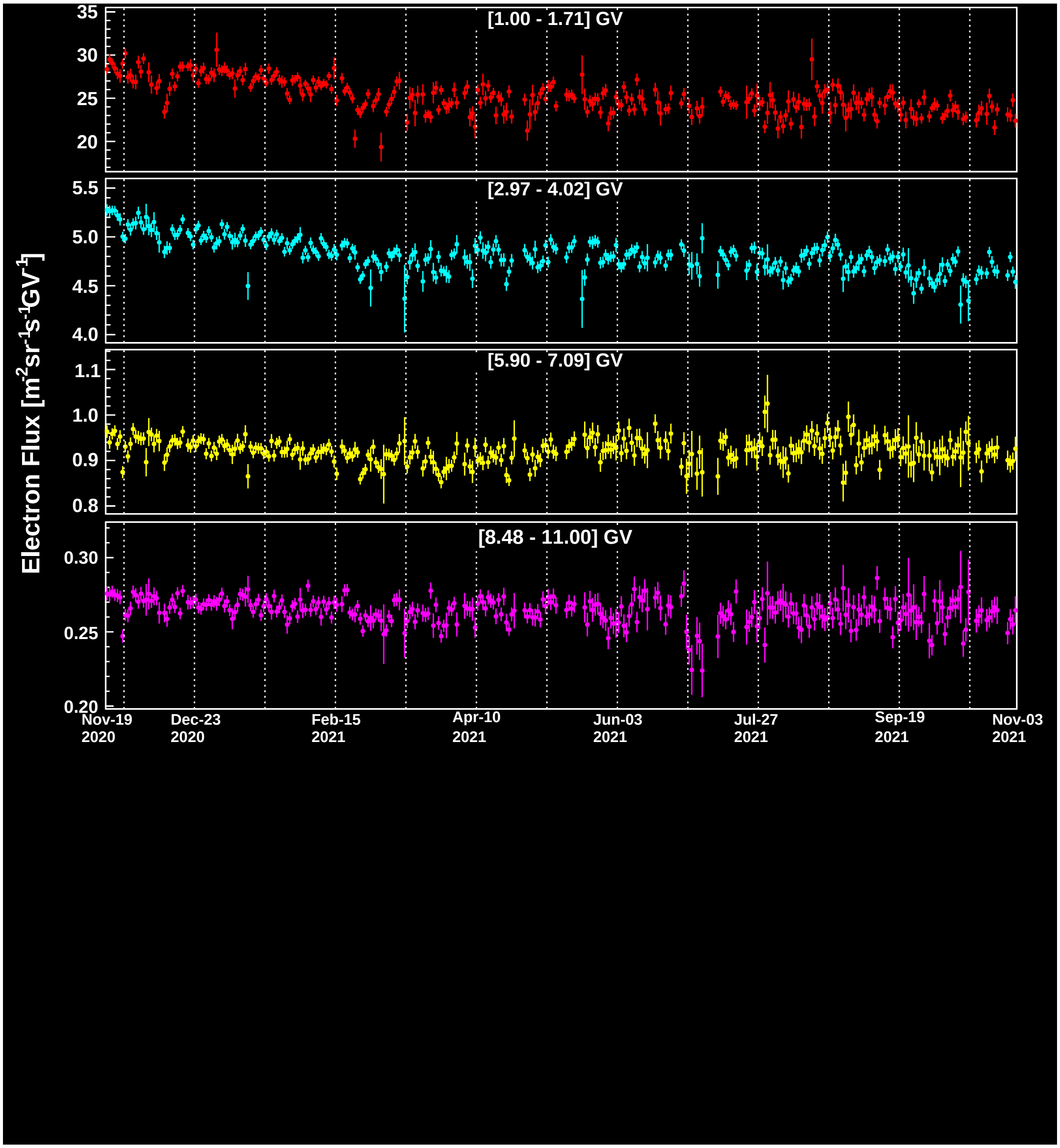

FIG. S18. The daily AMS electron fluxes measured from November 19, 2020 to November 2, 2021 for four rigidity bins. Vertical dashed lines separate Bartels rotations. Due to AMS upgrade, the 2021 data is not included in the periodicity analysis.

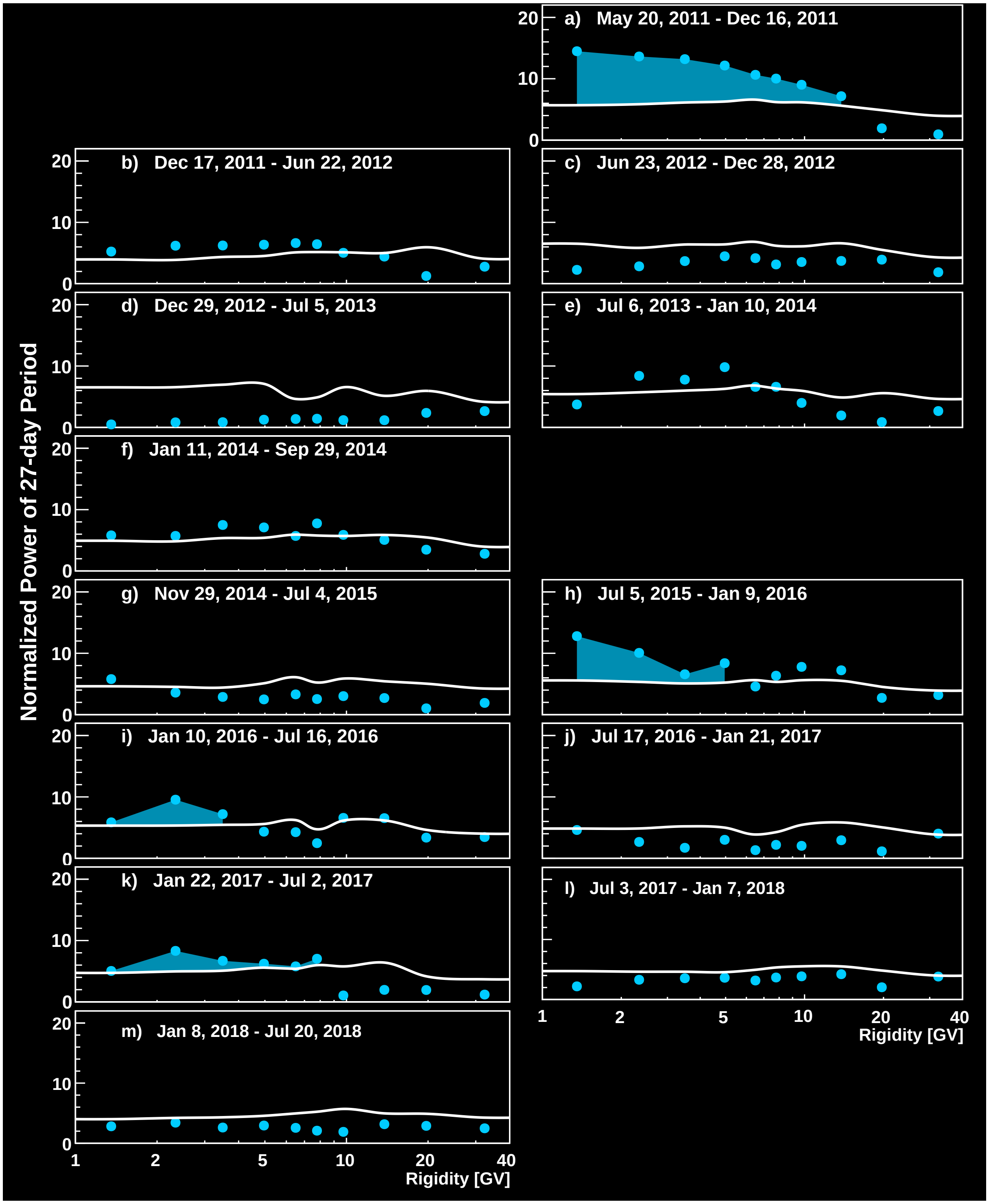

FIG. S19. The peak values of normalized power of the Φ_{e^-} wavelet analysis around 27 days (data points) as a function of rigidity for time intervals from 2011 to 2018. The curves indicate the 95% confidence levels. As seen, the 27-day periodicity is most prominent in (a) the second half of 2011, (h) the second half of 2015, (i) the first half of 2016, and (k) the first half of 2017, as indicated by the shaded areas. The rigidity dependence of the normalized power of 27-day period varies in different time intervals, but does not always decrease with increasing rigidity. Note, due to AMS upgrade, the periodicity analysis could not be performed for the data from the second half of 2018 to 2021.

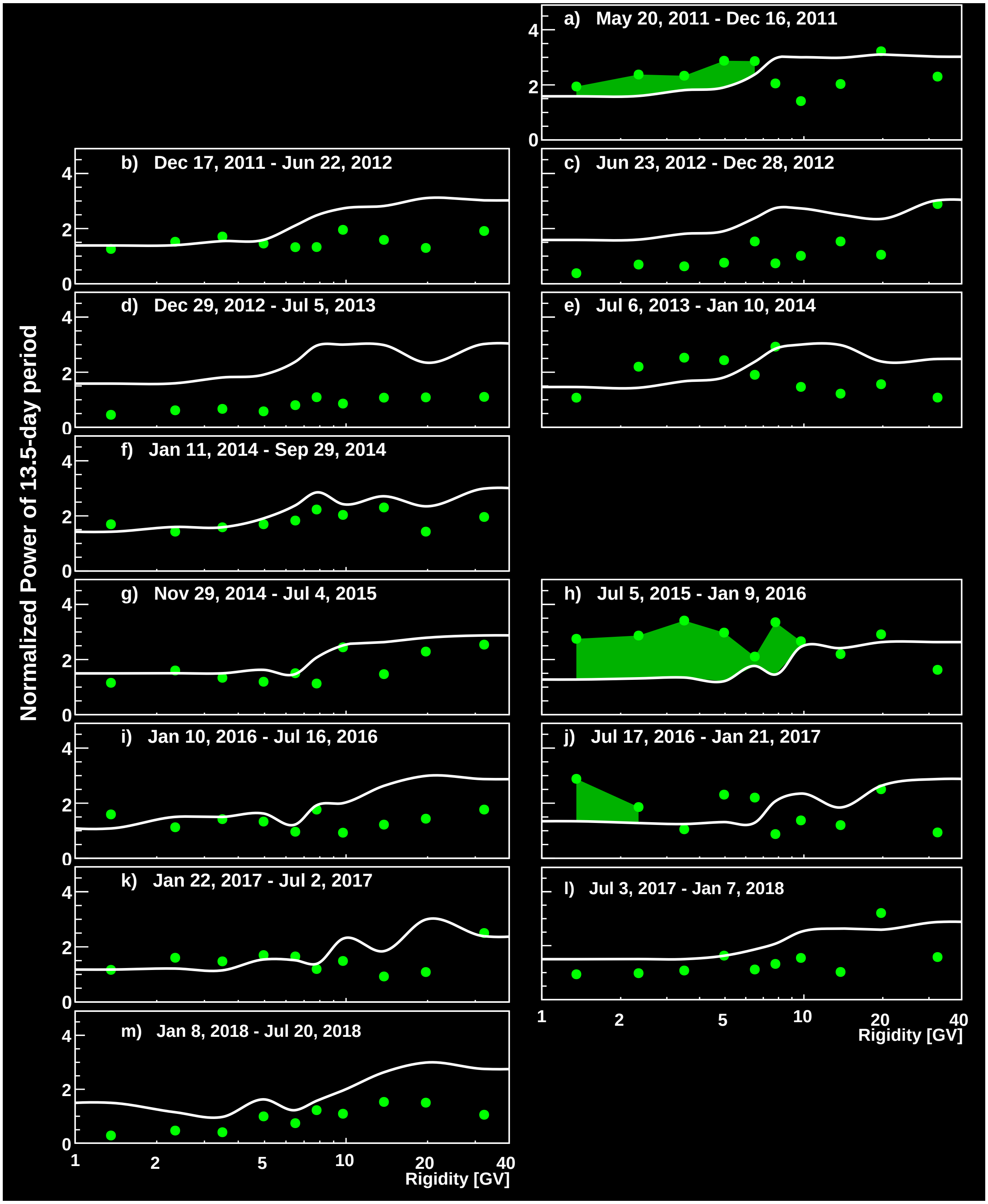

FIG. S20. The peak values of normalized power of the Φ_{e^-} wavelet analysis around 13.5 days (data points) as a function of rigidity for time intervals from 2011 to 2018. The curves indicate the 95% confidence levels. As seen, the 13.5-day periodicity is most prominent in (a) the second half of 2011, (h) the second half of 2015, and (j) the second half of 2016, as indicated by the shaded areas. The rigidity dependence of the normalized power of 13.5-day period varies in different time intervals, but does not always decrease with increasing rigidity. Note, due to AMS upgrade, the periodicity analysis could not be performed for the data from the second half of 2018 to 2021.

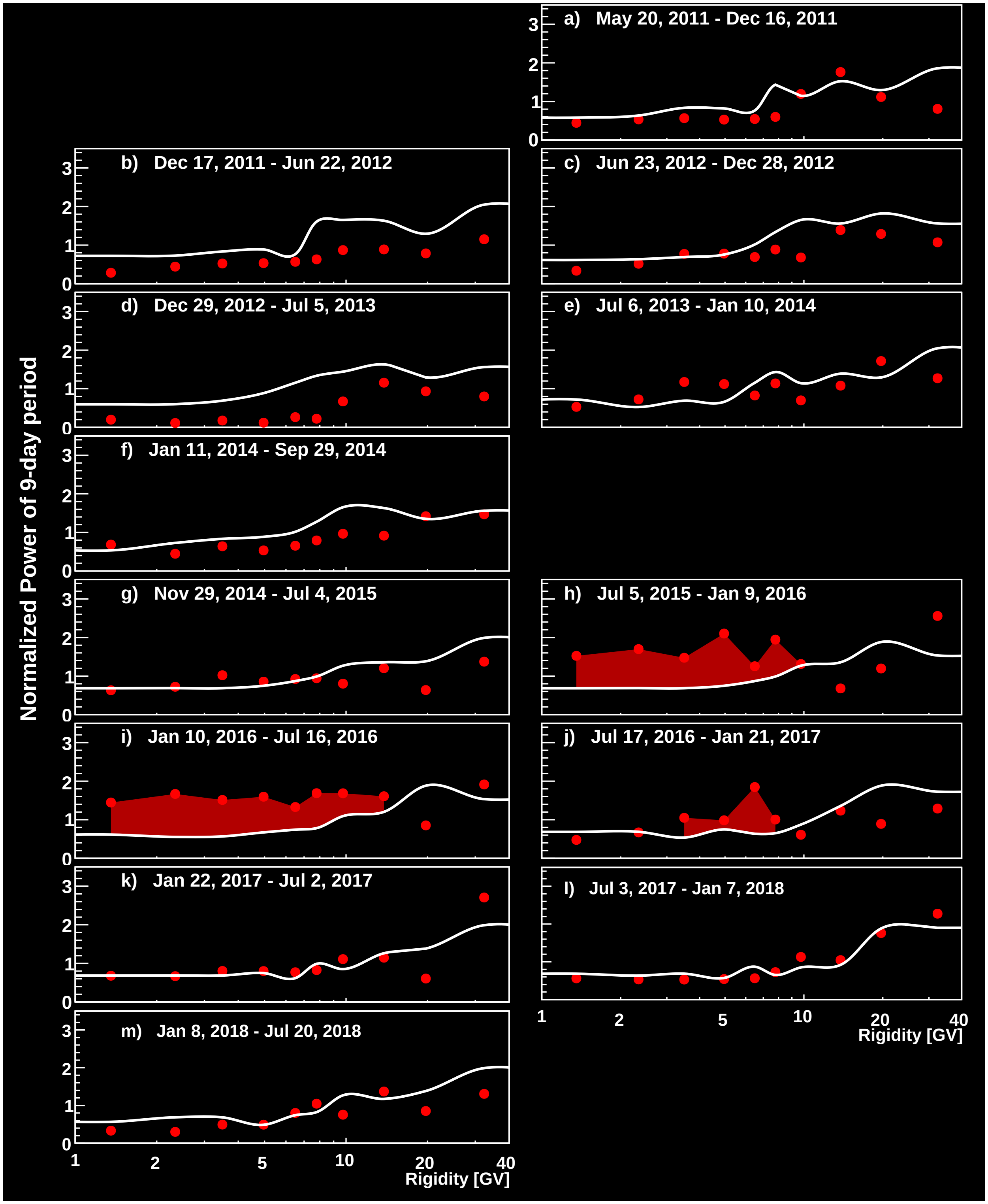

FIG. S21. The peak values of normalized power of the Φ_{e^-} wavelet analysis around 9 days (data points) as a function of rigidity for time intervals from 2011 to 2018. The curves indicate the 95% confidence levels. As seen, the 9-day periodicity is most prominent in (h) the second half of 2015, (i) the first half of 2016 and (j) the second half of 2016, as indicated by the shaded areas. The rigidity dependence of the normalized power of 9-day period varies in different time intervals, but does not always decrease with increasing rigidity. Note, due to AMS upgrade, the periodicity analysis could not be performed for the data from the second half of 2018 to 2021.

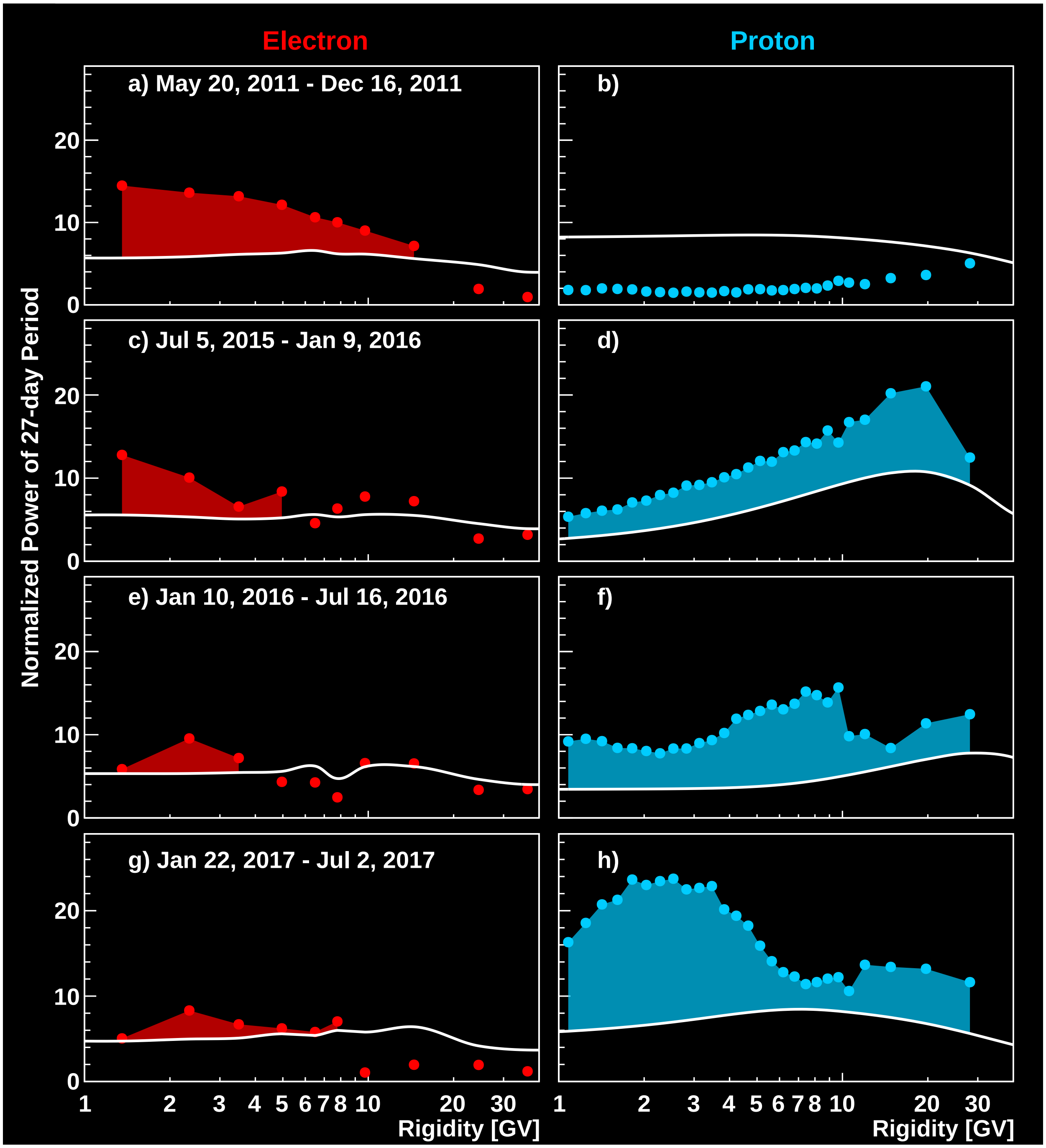

FIG. S22. The peak values of normalized power of wavelet analysis for Φ_{e^-} (left column) and Φ_p (right column) around 27 days (data points) as a function of rigidity during four time intervals: (a, b) May 20, 2011 – December 16, 2011, (c, d) July 5, 2015 – January 9, 2016, (e, f) January 10, 2016 – July 16, 2016, (g, h) January 22, 2017 – July 2, 2017. The curves indicate the corresponding 95% confidence levels. The shaded areas indicate the rigidity intervals where the periodicity is prominent. As seen, below 41.9 GV, the rigidity dependence of the normalized power of 27-day period are distinctly different between Φ_{e^-} and Φ_p.

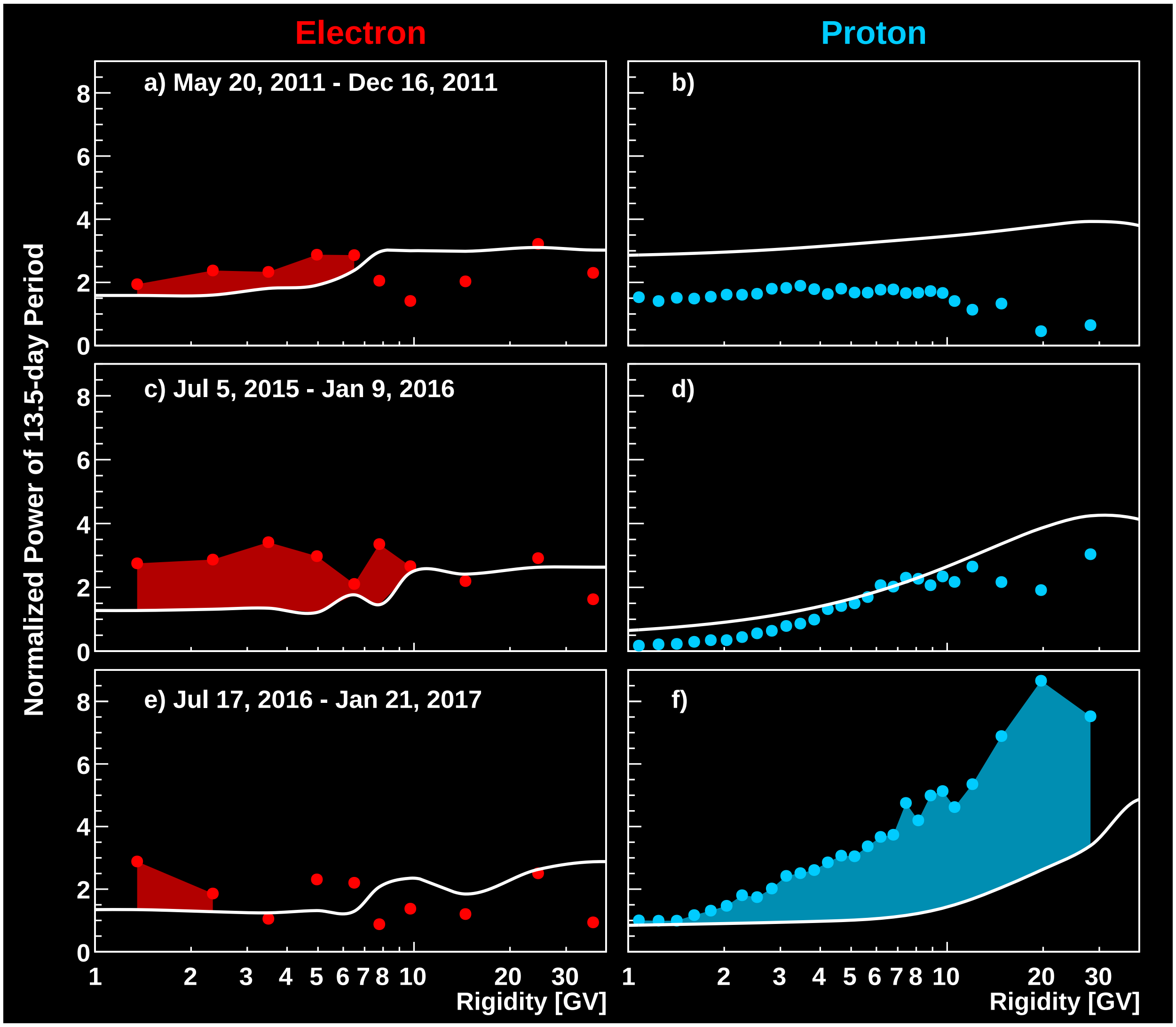

FIG. S23. The peak values of normalized power of wavelet analysis for Φ_{e^-} (left column) and Φ_p (right column) around 13.5 days (data points) as a function of rigidity during three time intervals: (a, b) May 20, 2011 – December 16, 2011, (c, d) July 5, 2015 – January 9, 2016, and (e, f) July 17, 2016 – January 21, 2017. The curves indicate the corresponding 95% confidence levels. The shaded areas indicate the rigidity intervals where the periodicity is prominent. As seen, below 41.9 GV, the rigidity dependence of the normalized power of 13.5-day period are distinctly different between Φ_{e^-} and Φ_p.

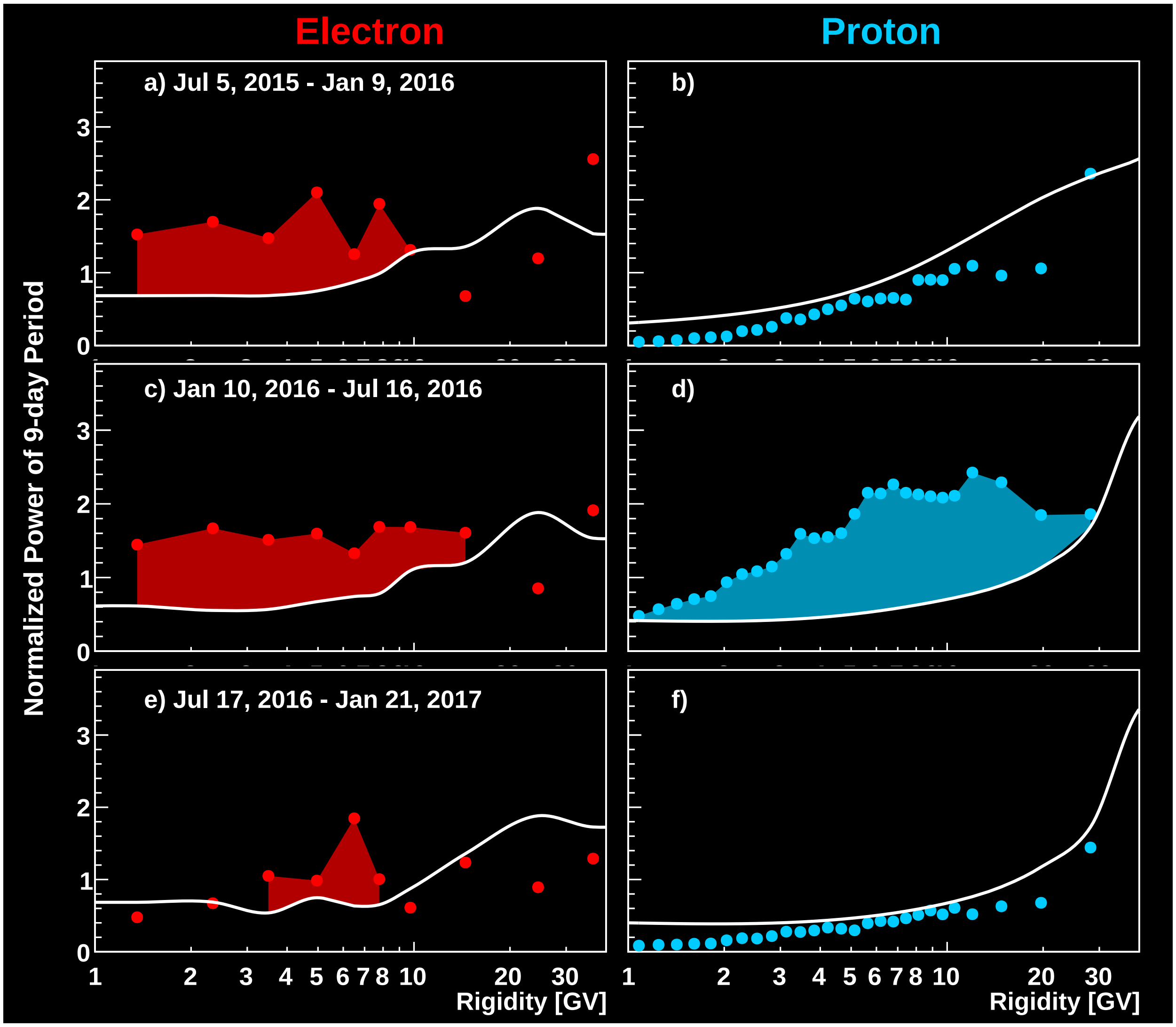

FIG. S24. The peak values of normalized power of wavelet analysis for Φ_{e^-} (left column) and Φ_p (right column) around 9 days (data points) as a function of rigidity during three time intervals: (a, b) July 5, 2015 – January 9, 2016, (c, d) January 10, 2016 – July 16, 2016, and (e, f) July 17, 2016 – January 21, 2017. The curves indicate the corresponding 95% confidence levels. The shaded areas indicate the rigidity intervals where the periodicity is prominent. As seen, below 41.9 GV, the rigidity dependence of the normalized power of 9-day period are distinctly different between Φ_{e^-} and Φ_p.

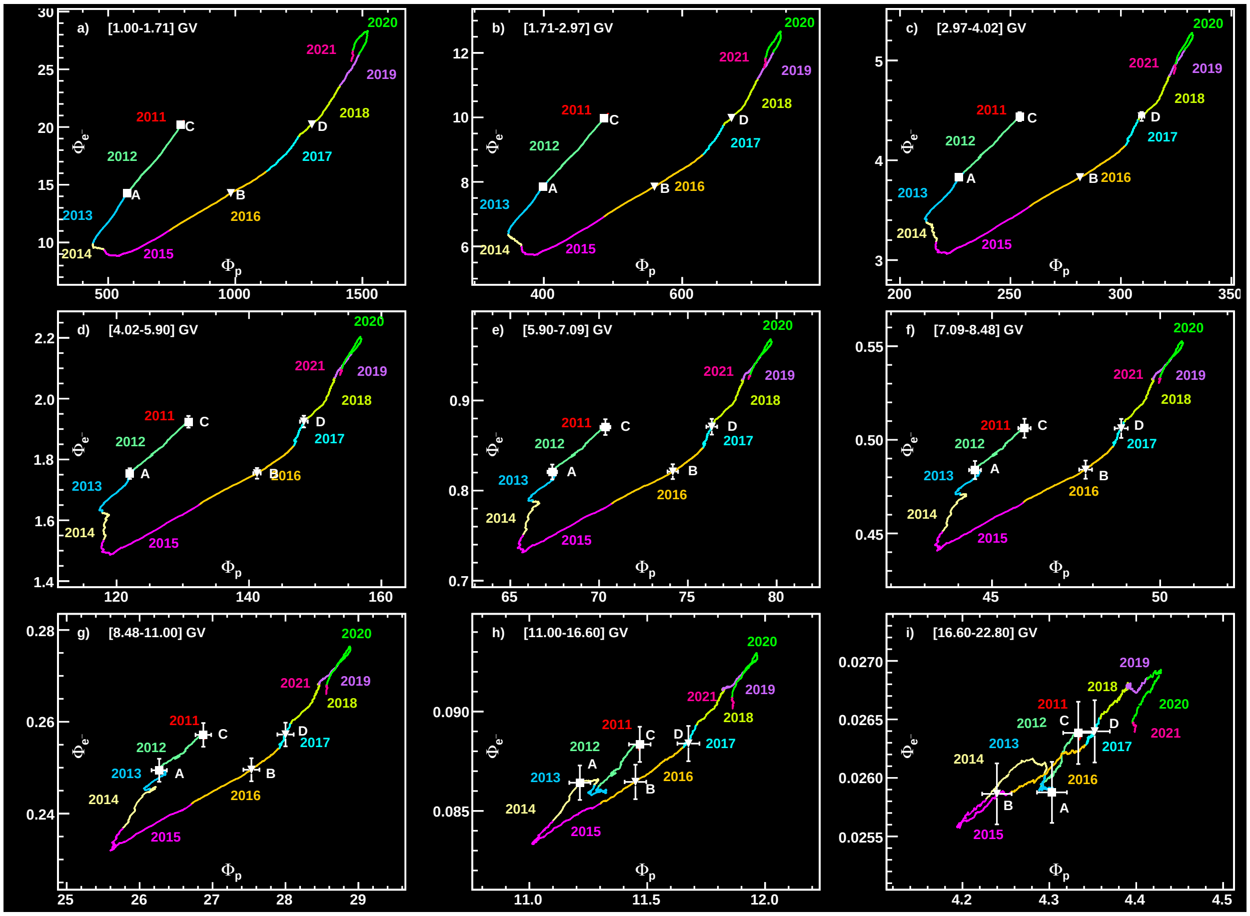

FIG. S25. Φ_{e^-} versus Φ_p both in units of [$m^{-2}sr^{-1}s^{-1}GV^{-1}$] for the rigidity bins from 1.00 to 22.8 GV both calculated with a moving average of 14 BRs with a step of one day. Different colors indicate different years from 2011 to 2021. The measured Φ_p for two pairs of time intervals of 14 BRs with the same Φ_{e^-} before the solar maximum in 2014-2015 (white squares, A and C) and after (white triangles, B and D) are shown. The horizontal and vertical error bars are the quadratic sum of the statistical and time dependent systematic errors of Φ_p and Φ_{e^-}, respectively.

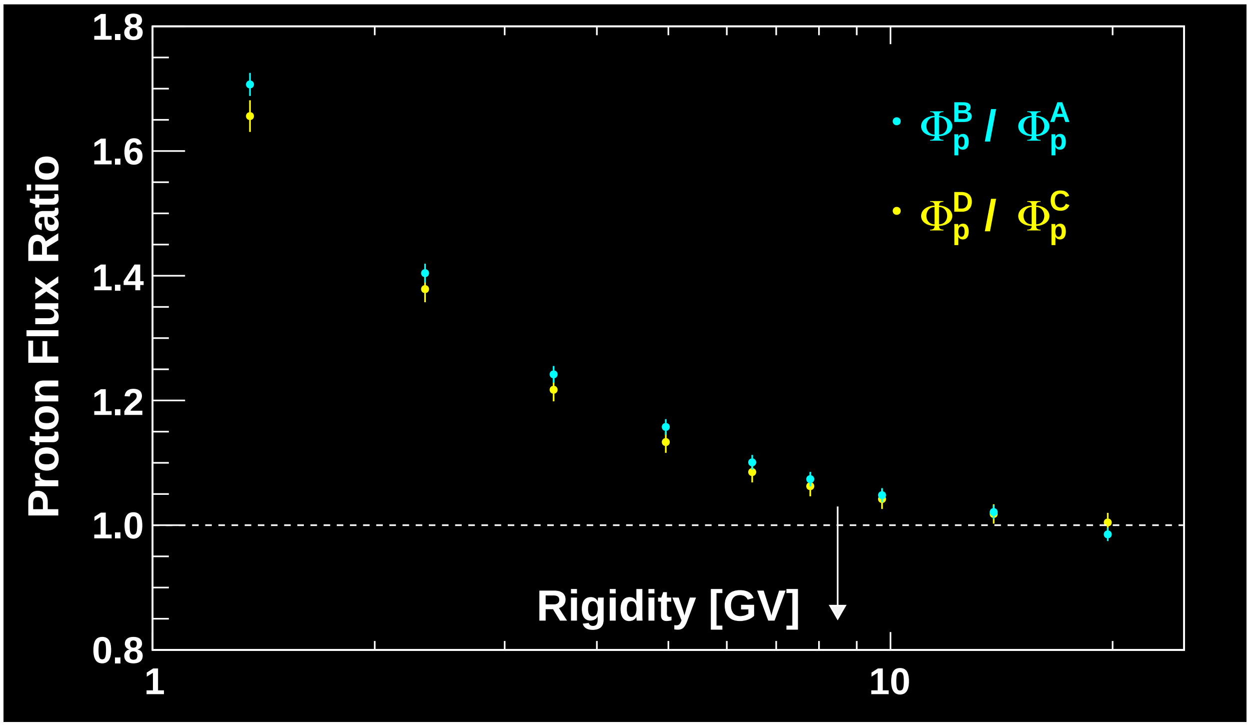

FIG. S26. The proton flux ratios Φ_p^B/Φ_p^A (cyan data points) and Φ_p^D/Φ_p^C (yellow data points) at two Φ_{e^-} as a function of rigidity from 1.00 to 22.8 GV (see Fig. S23). The error bars are the quadratic sum of the statistical and time dependent systematic errors of Φ_p and correlated errors from Φ_{e^-}. The horizontal dashed line indicates unity. Φ_p^B/Φ_p^A and Φ_p^D/Φ_p^C deviate from unity with a significance of 47σ at [1.00 – 1.71] GV, greater than 6σ below 8.48 GV (indicated by the arrow), and 4.1σ at [8.48 – 11.0] GV.

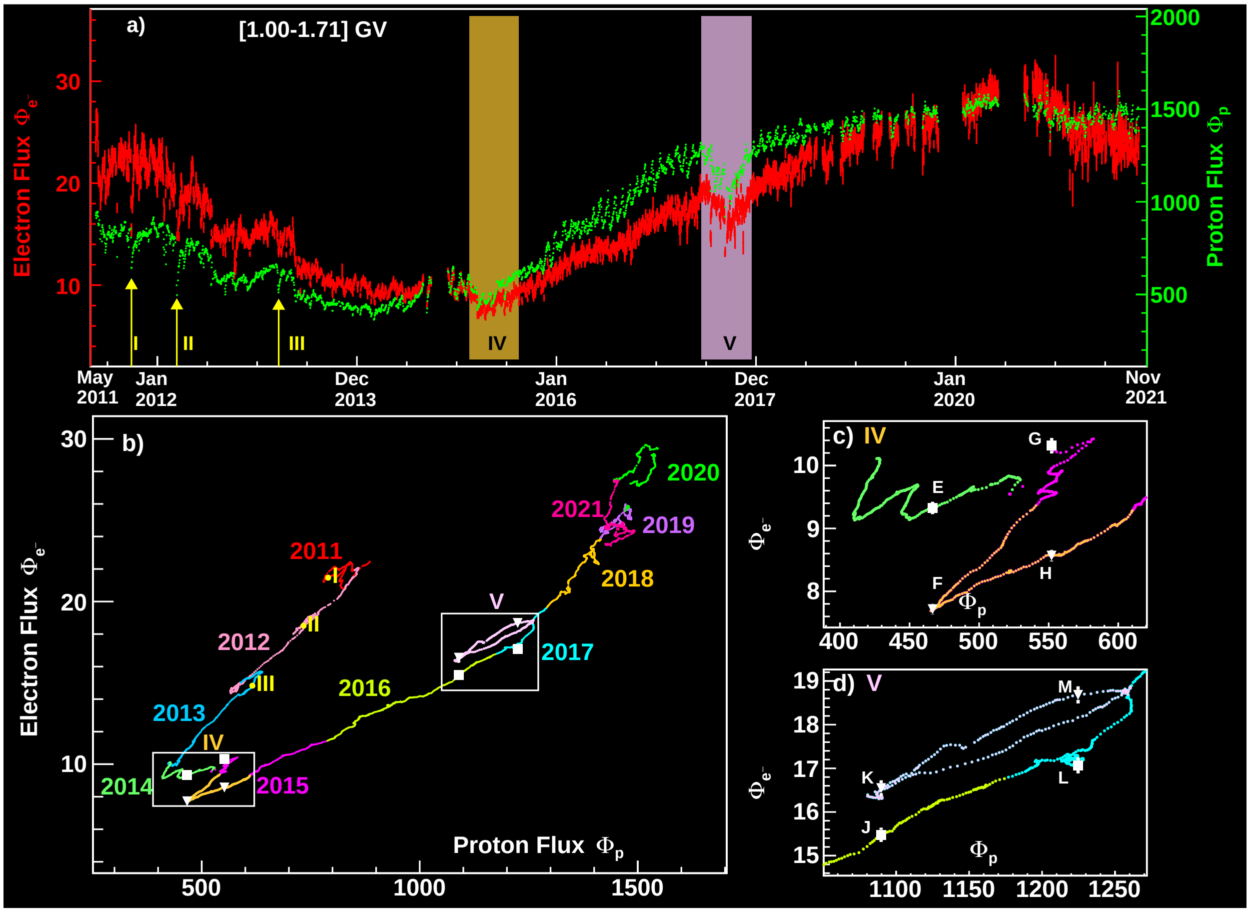

FIG. S27. (a) The daily electron fluxes Φ_{e^-} (red, left axis) and daily proton fluxes Φ_p (green, right axis) as a function of time for the rigidity interval of 1.00 to 1.71 GV. The arrows I, II, and III indicate the location of sharp dips in the proton and electron fluxes, and the colored bands IV and V mark the time intervals around the dips in 2015 and 2017. (b) Φ_{e^-} versus Φ_p both calculated with a moving average of 2 BRs and a step of 1 day. The location of I, II, and III correspond to the flux dips in (a). The dips in 2015 (IV) and 2017 (V) are indicated by white boxes. (c) To analyze the significance of the hysteresis structure in 2015, we select the two time intervals with the same Φ_p one in the first half (E) and one in the second half (F) of region IV, with the most significant difference in Φ_{e^-}. From this, we determine that the maximum difference is at $\Phi_p = 466.5$, the variation in Φ_{e^-} is $\Phi^F_{e^-}/\Phi^E_{e^-} = 0.827 \pm 0.013$. To obtain the overall significance of the hysteresis structure, we repeat the procedure for remaining non-overlapping time intervals of region IV and determine that the maximum difference is at $\Phi_p = 552.1$, indicated as G and H. The variation in electron flux is $\Phi^H_{e^-}/\Phi^G_{e^-} = 0.831 \pm 0.014$. Both $\Phi^F_{e^-}/\Phi^E_{e^-}$ and $\Phi^H_{e^-}/\Phi^G_{e^-}$ deviate from unity. The overall significance of the hysteresis structure corresponding to the dip in 2015 is 15.9σ. (d) The analysis is repeated for the dip in 2017 (V), with the four corresponding points J, K, L, M. The variation in Φ_{e^-} is $\Phi^J_{e^-}/\Phi^K_{e^-} = 0.935 \pm 0.015$ for $\Phi_p = 1089.7$, and $\Phi^L_{e^-}/\Phi^M_{e^-} = 0.914 \pm 0.015$ for $\Phi_p = 1224.7$. The significance of the corresponding hysteresis structure is 7.0σ. Fluxes are in units of $[\mathrm{m^{-2}sr^{-1}s^{-1}GV^{-1}}]$.

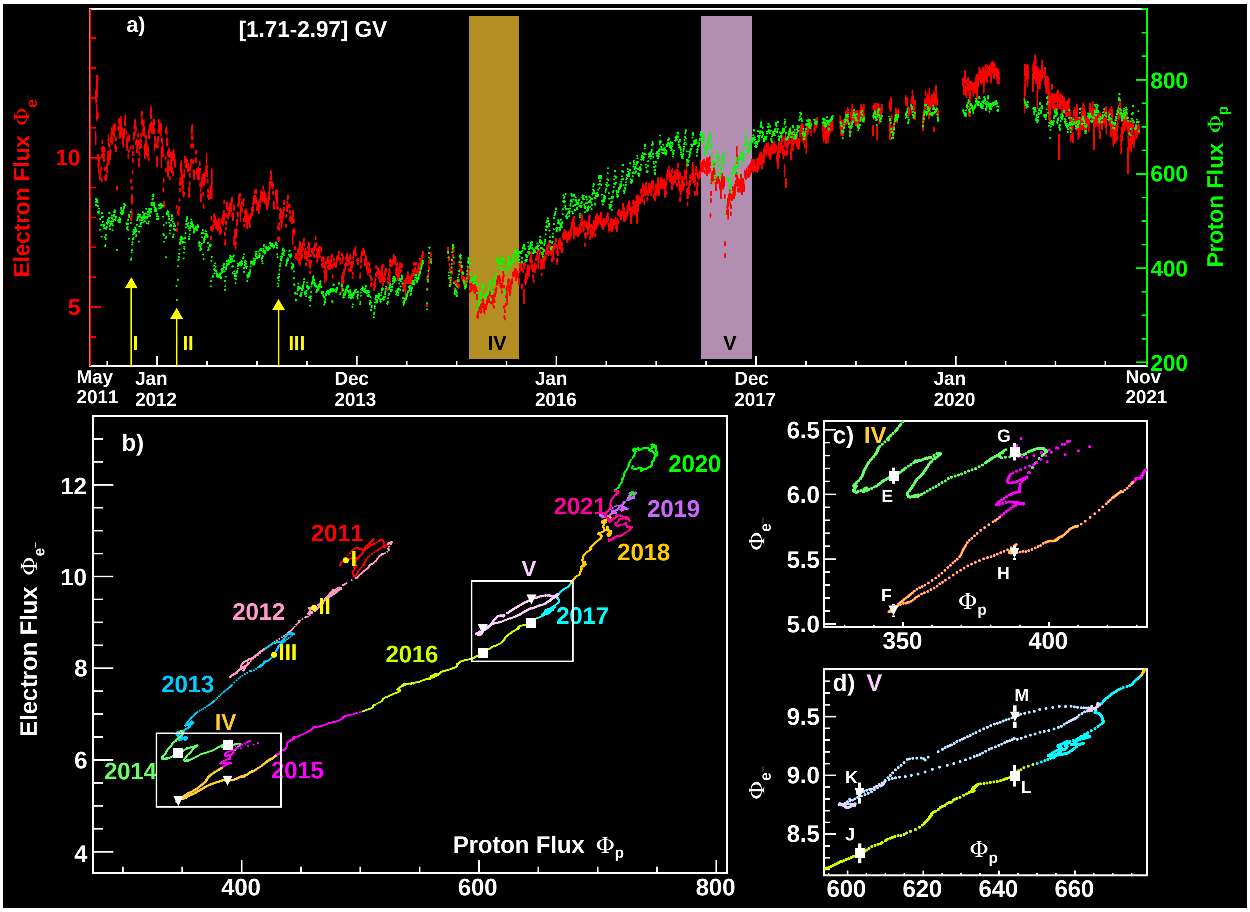

FIG. S28. (a) The daily electron fluxes Φ_{e^-} (red, left axis) and daily proton fluxes Φ_p (green, right axis) as a function of time for the rigidity interval of [1.71 – 2.97] GV. The arrows I, II, and III indicate the location of sharp dips in the proton and electron fluxes, and the colored bands IV and V mark the time intervals around the dips in 2015 and 2017. (b) Φ_{e^-} versus Φ_p both calculated with a moving average of 2 BRs and a step of 1 day. The location of I, II, and III correspond to the flux dips in (a). The dips in 2015 (IV) and 2017 (V) are indicated by white boxes. (c) To analyze the significance of the hysteresis structure in 2015, we select the two time intervals with the same Φ_p one in the first half (E) and one in the second half (F) of region IV, with the most significant difference in Φ_{e^-}. From this, we determine that the maximum difference is at $\Phi_p = 346.8$, the variation in Φ_{e^-} is $\Phi^F_{e^-}/\Phi^E_{e^-} = 0.831 \pm 0.013$. To obtain the overall significance of the hysteresis structure, we repeat the procedure for remaining non-overlapping time intervals of region IV and determine that the maximum difference is at $\Phi_p = 388.2$, indicated as G and H. The variation in electron flux is $\Phi^H_{e^-}/\Phi^G_{e^-} = 0.876 \pm 0.014$. Both $\Phi^F_{e^-}/\Phi^E_{e^-}$ and $\Phi^H_{e^-}/\Phi^G_{e^-}$ deviate from unity. The overall significance of the hysteresis structure corresponding to the dip in 2015 is 14.6σ. (d) The analysis is repeated for the dip in 2017 (V), with the four corresponding points J, K, L, M. The variation in Φ_{e^-} is $\Phi^J_{e^-}/\Phi^K_{e^-} = 0.942 \pm 0.015$ for $\Phi_p = 603.2$, and $\Phi^L_{e^-}/\Phi^M_{e^-} = 0.947 \pm 0.015$ for $\Phi_p = 644.1$. The significance of the corresponding hysteresis structure is 5.3σ. Fluxes are in units of [$\mathrm{m^{-2}sr^{-1}s^{-1}GV^{-1}}$].